Mechanisms for Extreme Precipitation Changes in a Tropical Archipelago

Daniel Argüeso, A. Di Luca, Nicolas Jourdain, R. Romero, V. Homar

HAL Id: hal-03874411
https://hal.science/hal-03874411v1

Submitted on 28 Nov 2022

Journal of Climate

Mechanisms for extreme precipitation changes in a tropical archipelago
--Manuscript Draft--

Manuscript Number:	JCLI-D-21-0224
Full Title:	Mechanisms for extreme precipitation changes in a tropical archipelago
Article Type:	Article
Corresponding Author:	Daniel Argüeso University of the Balearic Islands Palma, Baleares SPAIN
Corresponding Author's Institution:	University of the Balearic Islands
First Author:	Daniel Argüeso
Order of Authors:	Daniel Argüeso
	Alejandro Di Luca
	Nicolas C. Jourdain
	R. Romero
	V. Homar
Abstract:	The Maritime Continent is one of the most challenging regions for atmospheric models. Processes that modulate deep convection are poorly represented in models, which affects their ability to simulate precipitation features accurately. Thus, future projections of precipitation over the region are prone to large uncertainties. One of the key players in modelling tropical precipitation is the convective representation, and hence convection-permitting experiments have contributed to improve aspects of precipitation in models. This improvement creates opportunities to explore the physical processes that govern rainfall in the Maritime Continent, as well as their role in a warming climate. Here, we examine the response to climate change of models with explicit and parameterized convection and how that reflects in precipitation changes. We focus on the intensification of spatial contrasts as precursors of changes in mean and extreme precipitation in the tropical archipelago. Our results show that the broad picture is similar in both model setups, where islands will undergo an increase in mean and extreme precipitation in a warmer climate and the ocean will see less rain. However, the magnitude and spatial structure of such changes, as well as the projection of rainfall percentiles, are different across model experiments. We suggest that while the primary effect of climate change is thermodynamical and it is similarly reproduced by both model configurations, dynamical effects are represented quite differently in explicit and parameterized convection experiments. In this study, we link such differences to horizontal and vertical spatial contrasts and how convective representations translate them into precipitation changes.

23

Abstract

The Maritime Continent is one of the most challenging regions for atmospheric models. Processes that modulate deep convection are poorly represented in models, which affects their ability to simulate precipitation features accurately. Thus, future projections of precipitation over the region are prone to large uncertainties. One of the key players in modelling tropical precipitation is the convective representation, and hence convection-permitting experiments have contributed to improve aspects of precipitation in models. This improvement creates opportunities to explore the physical processes that govern rainfall in the Maritime Continent, as well as their role in a warming climate. Here, we examine the response to climate change of models with explicit and parameterized convection and how that reflects in precipitation changes. We focus on the intensification of spatial contrasts as precursors of changes in mean and extreme precipitation in the tropical archipelago. Our results show that the broad picture is similar in both model setups, where islands will undergo an increase in mean and extreme precipitation in a warmer climate and the ocean will see less rain. However, the magnitude and spatial structure of such changes, as well as the projection of rainfall percentiles, are different across model experiments. We suggest that while the primary effect of climate change is thermodynamical and it is similarly reproduced by both model configurations, dynamical effects are represented quite differently in explicit and parameterized convection experiments. In this study, we link such differences to horizontal and vertical spatial contrasts and how convective representations translate them into precipitation changes.

44

1   Introduction

48   The Maritime Continent (Fig. 1) is the largest archipelago on Earth and one of the most active

49   centers of deep moist convection on the planet. This tropical archipelago comprises thousands of

50   islands of varied sizes and steep topography surrounded by the Indo-Pacific Warm Pool, a region

51   with very high sea surface temperatures. Intense convective processes in the Maritime Continent

52   (MC) shape its precipitation regimes and thus have direct implications locally. However, the scale

53   and magnitude of convection is such that it helps transport large amounts of energy and moisture,

54   modulating global circulation patterns [*Neale and Slingo*, 2003; *Yamanaka et al.*, 2018]. Their

55   intrinsic relationship with phenomena such as the Madden-Julian Oscillation (MJO) [*Birch et al.*,

56   2016] and the Walker Circulation-ENSO [*Qian et al.*, 2010] are key examples of the interaction

57   across-scales that occur in the Maritime Continent.

58   The region has proven very challenging in terms of understanding and modelling precipitation

59   characteristics and the associated physical processes. Despite the importance of the region at

60   multiple scales, Global Climate Models fail to capture key features of the Maritime Continent such

61   as the MJO propagation [*Peatman et al.*, 2014; *Ling et al.*, 2019] and the diurnal cycle of rainfall

62   [*Baranowski et al.*, 2019], largely due to their coarse resolution. In fact, even the most recent

63   generation of GCMs (CMIP6) still show substantial biases in tropical precipitation [*Fiedler et al.*,

64   2020]. As a result, even though the CMIPs multi-model means suggest increases in rainfall over

65   the region (CMIP5: *Jourdain et al.* [2013] and Supplementary Figure S1; CMIP6: *Wang et al.*

66   [2020]), individual GCMs strongly disagree in the sign of rainfall changes [*Jourdain et al.*, 2013;

67   *Narsey et al.,* 2020].

68   Regional Climate Models (RCMs), which operate at higher spatial resolution, have contributed

69   to improve our understanding and simulation of the mechanisms underlying rainfall in the

70   Maritime Continent [*Vincent and Lane*, 2018; *Ruppert and Zhang*, 2019; *Li et al.*, 2020] through

71   better representation of fine-scale processes (i.e., sea-breeze, gravity waves, interaction across

72   scales, air-ocean fine-scale interactions). However, RCMs are still prone to substantial errors,

73   partly originated from the interaction between the convective representation and the land-sea

74   contrasts [*Birch et al.*, 2015; *Vincent and Lane*, 2017; *Im and Elthair*, 2018]. Models that explicitly

75   represent convection bring improvements in the simulation of the precipitation diurnal cycle but

76   produce unrealistic precipitation over steep topography [*Argüeso et al.*, 2016; 2020], misrepresent

77   the amplitude of the diurnal cycle [*Hassim et al.*, 2016, *Argüeso et al.* 2020] or introduce errors in

78   the rainfall modulation by the MJO phase [*Vincent and Lane*, 2017; *Wei et al.*, 2020]. The

79   challenges posed to models by convective processes in the MC have attracted much attention in

80   the recent years because of their central role in the climate at multiple scales. A perfect example

81   of this interest is the international initiative "Years of the Maritime Continent" (YMC Phase 1

82   2017-2020, *Yoneyama and Zhang* [2020]), aimed at coordinating international modelling and

83   observational efforts to advance our understanding of the MC weather-climate systems, and to

84   improve the representation of convective processes and precipitation in models.

85   Precipitation in the Maritime Continent tends to concentrate over the islands [*Qian*, 2008],

86   where rainfall is characterized by a strong diurnal cycle that most models struggle to capture. As

87   described by *Ruppert and Chen* [2020], the "island rainfall enhancement" effect and the land

88   precipitation diurnal cycle are ultimately linked to differences between land and ocean in surface

89   heat capacity and surface energy fluxes. They also show that the diurnal cycle of solar radiation

90   governs mesoscale circulations (i.e., land-sea and mountain-valley breezes), which in turn fuel the

4

91 convective development, help organize deep convection into mesoscale convective systems and

92 recharge the convective instability required for intense rainfall rates. Local steep topography

93 further contributes to organize convection by exciting and coupling with gravity waves and, in

94 certain situations, to reinforce it by inducing orographic lifting. These convective systems then

95 propagate offshore, assisted by gravity waves, reversed breezes (land breeze) and cold pools

96 [*Ruppert and Zhang*, 2019; *Yang et al.*, 2020], which together produce a diurnal cycle over water

97 that peaks between night and early morning, albeit generally weaker than over land. Therefore,

98 rainfall features in the MC strongly depend on local factors such as land-ocean contrasts,

99 mesoscale circulations, moisture convergence, intense convective instability, and topography.

100 In the context of climate change, we expect horizontal and vertical warming contrasts that may

101 induce changes in the intensity and spatial distribution of precipitation. For example, differences

102 in warming rates between continents and ocean can alter mesoscale circulations [*Joshi et al.*, 2007]

103 and vertical warming contrasts can modify atmospheric stability [*Wang et al.*, 2020], which will

104 likely affect rainfall in the Maritime Continent. At the ocean basin scale, thermal contrasts will

105 also play a key role in defining future changes of the Walker Circulation [*Yim et al.*, 2017] –and

106 hence in the El Niño-Southern Oscillation–, which ascending branch is anchored to the Maritime

107 Continent and likely modulated by the "island rainfall enhancement" effect [*Ruppert and Chen*,

108 2020]. At continental and seasonal scales, monsoons will be also intensified due to enhanced

109 thermal contrasts [*Seth et al.*, 2019], which may redistribute precipitation.

110 In the Maritime Continent, *Lambert et al.* [2017] did not find a consistent shift of rainfall from

111 ocean to land due to warming, as opposed to other tropical regions (i.e., Amazonia). *Bony et al.*

112 [2013] also identified land-sea thermal contrasts as having an important role in modifying tropical

113 rainfall patterns over land, although they deemed the dominant factor in tropical overturning

114 circulation to be the higher CO_2 concentrations and the resulting radiative imbalance in the

115 atmosphere. However, all these changes were established using Global Climate Models (GCMs),

116 which have serious difficulties in representing crucial features of the Maritime Continent rainfall

117 [*Jourdain et al.,* 2013; *Schiemann et al.*, 2013; *Baranowski et al.*, 2019; *Yang et al.*, 2020]. Recent

118 studies have generated future climate projections using RCMs [*Supari et al.,*2020*; Tangang et al.,*

119 2020] and found that both increases and decreases in land precipitation over areas of the MC were

120 plausible, depending on the region and the season examined. Yet, the physical mechanisms driving

121 such changes have not been explored.

122 Therefore, the use of higher-resolution models to better understand the mechanisms driving

123 future changes in precipitation over the region is still necessary. Despite some errors that persist

124 in high-resolution models, experiments that explicitly resolve convection are especially beneficial

125 in coastal areas, regions of complex topography and locations with frequent and intense deep

126 convection [*Prein et al.*, 2015; Lucas-Picher et al. 2021], all of which apply to the Maritime

127 Continent. In this study, we use a model at convection-permitting scales to investigate the response

128 of rainfall to a warming climate. For the first time, we examine future climate information at

129 convection-permitting scales in the entire Maritime Continent and determine the different response

130 of rainfall extremes to climate change in parameterized and explicit convection experiments. We

131 also conducted a novel analysis of the role of warming spatial contrasts, land-sea breeze

132 circulations and modified atmospheric stability in modulating this response. We expect that land-

133 sea thermal contrast changes will affect breeze circulations, and vertical differences in the response

134 to global warming will modify vertical profiles and stability. In combination, they will have

135 implications for future climate precipitation regimes in the region. Since the interactions between

136 convection and the environment are represented differently in explicit and parameterized

137   convection models, precipitation responses to climate change will likely differ between these

138   models too. In view of this possibility and the expectations around convection-permitting models

139   for future projections [*Fosser et al.*, 2020; *Prein et al.*, 2020; Lucas-Picher et al. 2021], we explore

140   the rainfall response to increased temperature in both explicit and parameterized convection

141   experiments at very high resolution.

142   The rate at which precipitation responds to surface temperature changes is known as

143   precipitation scaling [*Trenberth*, 1999; *Held and Soden*, 2006] and has two main components:

144   dynamical and thermodynamical (see Box 11.1 in *Seneviratne et al.* [2021]). In the past, also the

145   co-variational term was explored [*Bony et al.* 2004]. The thermodynamical component is linked

146   the Clausius-Clapeyron relationship –increased atmospheric water-holding capacity with

147   temperature– and is a primary mechanism for climate-scale precipitation changes. Under climate

148   change conditions, this should contribute to more intense precipitation rates, particularly for

149   extremes [*Dobrinski et al.* 2018]. The dynamical component includes changes in large-scale

150   circulation patterns that determine the supply of moisture and in local circulations that contribute

151   to vertical motions. The intensification of sea-breeze, atmospheric instability and convective

152   processes is framed in the latter group (i.e., local circulations). Here, we focus on the role of local

153   circulations to explain the spatial patterns of precipitation changes, which is related to the

154   dynamical part. However, we also explore the contribution of thermodynamical changes to provide

155   a comprehensive picture. We examine the separate contribution of thermodynamical and

156   dynamical mechanisms to intense precipitation changes in the region and we identify differences

157   between parameterized and explicit convection models in this context.

2 Methods

2.1 Model and present-climate experiments

In this study, we use the Weather Research and Forecasting (WRF) Model v3.9.1 [*Skamarock et al.*, 2008] to simulate the atmosphere over the Maritime Continent and investigate rainfall patterns under climate change conditions. The model was run at 4-km spatial resolution over a domain covering 5916 km by 2556 km (1479 by 639 grid points) in the Maritime Continent and resolving the vertical with 50 hybrid coordinate levels. The experiments span three consecutive austral summers (1st November to 1st March; 2013-2014, 2014-2015 and 2015-2016), each preceded by a 10-day spin-up period (22nd October – 31st October) that was discarded in the analysis. The analysis period covers the wet season for most of the Maritime Continent and the selected years span both positive and negative phases of the El Niño/Southern Oscillation.

The physical parameterization schemes are among the most widely used options and were chosen according to previous studies over the region [*Li et al.*, 2016; *Argüeso et al.*, 2016; *Vincent and Lane*, 2017]. The setup consists in the WRF single moment 6-class microphysics scheme [WSM6; *Hong and Lim*, 2006], the Yonsei University (YSU) scheme for Planetary Boundary Layer turbulence, the Rapid Radiative Transfer Model scheme for longwave radiation (RRTM), the Goddard scheme for shortwave radiation, the Noah land surface model and the MM5 similarity scheme for the surface layer. In the parameterized convection experiment, the Betts-Miller-Janjic [BMJ; *Betts and Miller*, 1986, 1993; Janjic, 1994] scheme was chosen to represent both deep and shallow convection, while it was turned off for the explicit convection experiment (see *Argüeso et al.* [2020] for additional details on the model configuration). In this framework, clouds are driven by the microphysics parameterization regardless of the convective representation. However, the environmental conditions in the model will depend on the convective representation and thus the

181 microphysics scheme will likely generate different clouds. In the explicit simulations, it is the

182 model equations (dynamical core) that represent convection and its effects on the atmosphere

183 vertical profile. In the parameterized runs, the BMJ scheme does not directly inhibit explicit

184 convection, but it reduces the potential for explicit convection because it removes energy from the

185 atmosphere through the adjustment towards a stable vertical profile. Explicit convection at scales

186 resolved by the model grid is still possible though, especially in environments that favor strong

187 convective processes.

188 Present climate experiments are directly initialized and driven by ERA5 reanalysis [*Hersbach*

189 *et al.* 2020] at circa 0.3° spatial resolution and updated every 6 hours. *Argüeso et al.* [2020] already

190 analyzed these simulations and compared them against satellite-derived products to examine the

191 role of different convective representations and the spatial resolution in representing realistic

192 rainfall features. They concluded that, as opposed to higher resolution experiments, 4-km provides

193 the best estimates of precipitation while maintaining computational and storage costs affordable.

194 This is the upper boundary of the convective grey zone [*Prein et al.,* 2015], a range of spatial

195 resolutions (~4-10km) where explicit and parameterized convection may compete. It is yet unclear

196 whether convection should be parameterized in this range. Thus, it further justifies the analysis of

197 both parameterized and explicit convection setups.

198 **2.2   Pseudo Global Warming experiments**

199 This study expands the existing set of runs in *Argüeso et al.* [2020] by incorporating Pseudo

200 Global Warming (PGW, [*Schär et al.* 1996]) experiments to examine the response of rainfall to a

201 particular climate change signal. These experiments were built adding the climate change signal

202 obtained from a global climate multi-model ensemble from the Coupled Inter-comparison Model

203 Project Phase 5 (CMIP5). We calculated the seasonal cycle of all variables ingested by the model

204 (i.e., wind components, humidity, geopotential height and temperature at pressure levels; and 2-m

205 dew-point temperature, 2-m temperature, 10-m wind components, surface pressure, mean sea level

206 pressure, and sea surface temperature) for historical (1989-2009) and future (2080-2100) climate

207 experiments from 33 GCMs (Supplementary material). We computed the climate change signal

208 for each calendar month, each variable, and each model, and interpolate them to a common 0.72°

209 grid to calculate a multi-model mean climate change signal. These monthly changes are linearly

210 interpolated in time to 6-hourly intervals and nearest-neighbor interpolated to the ERA5 grid. Then

211 they are added to ERA5 to create the initial and boundary conditions to drive WRF under a

212 synthetic future climate scenario. The PGW method has been previously evaluated in a "perfect

213 model approach" with satisfactory results [*Yoshikane et al.,* 2012; *Donat-Magnin et al.,* 2021] and

214 was applied in a wide range of studies from tropical cyclones [*Chen et al.,* 2020] to ice sheets

215 [*Donat-Magnin et al.,* 2021].

216 The future climate change signal is here represented by the Representative Concentration

217 Pathway 8.5 (RCP8.5 scenario). We chose this high-emission scenario to examine the impact of a

218 marked climate change signal on the Maritime Continent, but this choice does not imply any

219 assumptions on its likeliness.

220 Even though this experiment set up does not constitute a rigorous future climate projection and

221 thus has limitations, it offers numerous advantages. While runs are not long enough to be

222 completely representative of the climate, their duration is a very good reason to force future climate

223 runs with climatological anomalies from the GCMs multi-model ensemble (MMM). This way, our

224 results are less dependent on the interannual variability produced by individual models for specific

225 years. Furthermore, it is often argued that changes projected by the MMM are in general more

226 credible than projections produced by individual models [*Knutti et al.,* 2010]. In addition, CMIP5

227 models' biases are stationary even under strong climate changes [*Krinner and Flanner, 2*018],

228 hence this method partly overcomes the biases in the climate states produced by individual models.

229 The MMM estimates are still subjected to biases, such as the Sea Surface Temperature warming

230 patterns that require complex bias-correction methods [*Dutheil et al.*, 2020], but the same applies

231 to direct downscaling of individual highly biased GCMs. The PGW method includes the

232 thermodynamical effects produced by a given climate change signal and some dynamical features.

233 For example, it considers the mean change in the large-scale dynamics because the geostrophic

234 balance is linear. However, it misses changes in the structure and variability of circulation patterns,

235 as well as some non-linear large-scale dynamics and variability. These include phenomena such

236 as MJO or ENSO, some of which may undergo frequency changes in the future [*Cai et al.,* 2018].

237 Another potential limitation is that non-stationary biases that may be shared by CMIP5 models are

238 not removed with the multi-model mean. It is important to note that these features can affect the

239 spatial patterns of precipitation changes in our experiments.

240 Overall, the method constitutes an interesting, efficient, and solid approach to quantify the

241 response of the climate change system to plausible future conditions. It also brings the analysis

242 down to the physical-process level at feasible computational costs, especially considering the

243 demands of convection-permitting experiments at continental scales. In this study, we refer to the

244 PGW simulations as "future" experiments for clarity reasons. Changes projected by the selected

245 multi-model ensemble over the Maritime Continent are shown in the supplementary material

246 (Supplementary Figure S1) for temperature, wind, precipitation, and integrated water vapor.

247   **2.3   Scaling calculation**

248 We first calculate the scaling of extreme precipitation with temperature directly from the model

249 outputs. To further understand the underlying mechanisms, we also calculate changes in

250   precipitation extremes using the physical scaling diagnostic described in *O'Gorman and*

251   *Scheneider* [2009b], which estimates precipitation rates from vertical profiles of vertical pressure

252   velocity, temperature, and pressure. This methodology is usually applied to high-percentile

253   precipitation events by selecting times when they occur. It expresses the precipitation rate during

254   an extreme event at each grid point as:

$$P_e \sim - \left\{ \omega_e \left. \frac{dq_s}{dp} \right|_{\theta^*, T_e} \right\}$$

Eq. 1

255   Where P_e is the precipitation amount during an extreme event, ω_e is the corresponding vertical

256   pressure velocity, $\{\cdot\}$ is a mass-weighted integral over the troposphere, and the remainder is the

257   vertical derivative of the saturation specific humidity q_s at constant saturation equivalent potential

258   temperature θ^* (i.e., moist adiabatic) and evaluated at the mean temperature T_e during the intense

259   rainfall event (See *O'Gorman and Scheneider* [2009b] for additional details). By comparing

260   estimates from present- and future-climate experiments, it is possible to approximate the full

261   precipitation scaling for extremes, which aggregates the effects of thermodynamic and dynamic

262   processes.

263   Following *Pfahl et al.* [2017], we can decompose changes in heavy rainfall into thermodynamic

264   and dynamic contributions. To calculate the separate effect of thermodynamic processes, we

265   ignore changes in the vertical profile of ω_e and we use instead the time-average from present

266   climate experiments calculated only for extreme precipitation hours ($\overline{\omega_{e\_present}}$). The new heavy

267   rainfall estimates (P_{e_thermo}, Eq. 2) will be due to changes in the vertical derivative of q_s only. The

268   dynamic contribution (P_{e_dyn}, Eq.3) is calculated by subtracting the thermodynamic scaling (Eq 2)

269   from the full scaling (Eq. 1).

$$P_{e\_thermo} \sim - \left\{ \overline{\omega_{e\_present} \frac{dq_s}{dp} \bigg|_{\theta^*, T_e}} \right\}$$

Eq. 2

$$P_{e\_dyn} = P_e - P_{e\_thermo}$$

Eq. 3

270

271   In this study, we apply for the first time this diagnostic to convection-permitting experiments

272   and hourly model outputs to disentangle the contribution of thermodynamic and dynamic

273   processes and explain possible deviations from the Clausius-Clapeyron relationship at very high

274   spatiotemporal scales. Prior to applying the scaling, we horizontally smoothed the vertical pressure

275   velocity (ω_e) – not the vertical derivative of q_s – using a gaussian filter with a standard deviation

276   of 20 km. Reasons for this include: 1) to reduce the effect of downdrafts produced by intense

277   rainfall within the convective cell and characterize the environment producing the extreme

278   episode, 2) to filter out the influence of single-cell storms that models may generate at these scales

279   [*Murata et al.,* 2017a] and 3) to better match the scales previously used with this method (~100

280   km) [*Pfahl et al.*, 2017]. Scaling was also calculated without any prior spatial smoothing.

281   **3   Results**

282   **3.1   Precipitation changes in explicit and parameterized convection models.**

283   In this section, we analyze changes in mean precipitation as simulated by the parameterized

284   (PA) and explicit (EX) convection experiments. We compare present and future experiments over

285   three consecutive austral summers (NDJF) and calculate changes relative to present-climate values

286   ([future-present]*100/present). Mean precipitation changes show a prominent contrast between a

287   net increase over land and a decrease over the ocean (Fig. 2). Both model configurations simulate

288   a domain-average decrease in mean precipitation (-13.3% for PA and -6.2% for EX), probably

13

289   because they are driven by the same boundary conditions, which exert control over the large-scale

290   dynamics. The MMM of the CMIP5 ensemble used here to create the PGW scenario project a

291   slight increase in the domain-average rainfall (4.9%), but precipitation is a model prognostic

292   variable and is not used to generate the boundary conditions. While this difference in the sign of

293   changes may seem contradictory, the link between the large-scale conditions and precipitation in

294   models is complex. Factors that contribute to this disparity include differences in the spatial scale

295   (grid-averaging effects), in the efficiency of convective schemes, in the response of convective

296   schemes to environmental changes and in surface evapotranspiration. Furthermore, the CMIP5

297   ensemble projects a wide range of possible changes over the domain (between -16.6% and 19.8%).

298   Despite these differences and the divergence across CMIP5 models [*IPCC*, 2013; and

299   Supplementary Figure S1], the ensemble consistently projects larger increases over land than over

300   the ocean, which is coherent with our results (Fig. 2).

301   Both our experiments produce an increase in rainfall over land (4.3% PA; 5.0% EX) and a

302   decrease over the ocean (-20.2% PA; -12.7% EX). Narrow waters in between islands and coastal

303   areas are notable exceptions to this general response. Thus, according to our experiments, a warmer

304   atmosphere would generate more rainfall over land in the Maritime Continent, although the spatial

305   variability is large over both land and ocean (Fig. 2e). Changes are similar across all three austral

306   summers in the PA runs and results from one year deviate from the other two in the EX run (Fig.

307   2e and Supplementary Figure S2). Altogether, this provides confidence on the robustness of the

308   results.

309   The spatial pattern of precipitation changes is broadly similar in both experiments, but there are

310   features in the response that differ between the two. Firstly, the magnitude of changes: PA

311   produces larger decreases of rainfall over the ocean. Secondly, EX experiments are spatially

312 noisier and so is the response to warming. This is partly explained by the length of the simulations,

313 but PA is spatially much smoother, which suggests that the noise is inherent to how convective

314 processes are represented. In fact, changes in EX shows a larger year-to-year variability than PA

315 under the same large-scale conditions (Fig. 2e). This contrast is relevant because the next

316 generation of climate projections will shift towards convection-permitting models [*Prein et al.,*

317 2015, 2020], which may produce less spatially homogeneous projections if they behave like our

318 model. None of the two model projections can be deemed more likely than the other because their

319 relative performance varies depending on the metric analyzed [*Argüeso et al.,* 2020]. However,

320 explicit convection brings increased realism of precipitation features often misrepresented in

321 models such as the diurnal cycle and its coupling with the land-sea breeze [*Birch et al.*, 2015;

322 *Argüeso et al.*, 2020].

323 In addition to mean precipitation, we analyze the model extreme precipitation response to a

324 climate change signal and quantify the role of convective representation in that response (Fig. 3).

325 We characterize changes in precipitation events through a range of percentiles (50th to 99.9^{th}) and

326 focus on the upper tail of the distribution (95th, 98th, 99th and 99.9^{th} percentiles). The statistical

327 significance of changes was tested at the 90% confidence level using a bootstrapping approach

328 based on resampling with replacement following *Contractor et al.* [2018, 2021]. For each grid

329 point, we concatenated present and future, and resampled the resulting timeseries with replacement

330 under the null hypothesis that there is no change. The same permutation is used for all grid points

331 to preserve spatial dependence in the resampled data. The resampling was done using 12-hour

332 blocks to preserve temporal dependence of events. This assumes independence of rainfall from

333 one 12-hour period to the next, which is supported by the distinct diurnal cycle of rainfall in the

334 region. The diurnal cycle was considered when defining the blocks (06-18UTC and 18-06UTC)

335   so that the rainfall peak at around 5pm LST is not split across two blocks. This approach neglects

336   correlation in rainfall on daily or longer timescales, which could lead to some overestimation in

337   the number of independent samples.

338   We split the resampled timeseries in two equal parts and calculate the change in the percentiles

339   between the two. The process was repeated 1000 times to build a distribution of quantile change

340   ratios between the two, which is normally distributed around 0, and estimate the p-values of the

341   original quantile change ratios. Percentiles were calculated for each grid point and each period

342   (present and future) separately. Percentiles can be calculated using all hourly values [*Schär et al.,*

343   2016] or wet-only values [*Chan et al.,* 2016] depending on the purpose of the analyses. While both

344   may have advantages, we chose the all-hourly values approach because having a fix population of

345   events ensures that: a) changes in each percentile univocally means that events exceeding that

346   percentile (extreme) must change, b) upper percentiles are not affected by changes in light rain

347   frequency, and c) percentiles represent a fixed number of events at all locations, runs and periods.

348   For instance, the upper percentiles we focus on represent circa 433, 173, 87, and 9 hourly events

349   in all grid cells and all experiments. These advantages make our results easier to interpret in the

350   context of this study. Present climate values of these percentiles are provided in the supplementary

351   material (Supplementary Figure S3). Changes in percentiles using wet-only values (>0.1 mm hr^{-1})

352   are shown in Supplementary Figure S4 for comparison with the all-hourly values approach.

353   Changes in wet-only percentiles are comparable to higher percentile changes using all-hourly

354   values. This is because wet-only percentiles characterize a higher section of the rainfall distribution

355   tail. Although changes in wet-only percentiles are affected by changes in the entire distribution of

356   rainfall, the spatial patterns between the two approaches are very similar for very intense

16

357   precipitation events. They both show a land-sea contrast. Differences between PA and EX are also

358   similar using one approach or another.

359   Domain-average changes of precipitation percentiles are summarized in Table 1 along with

360   separate changes over land and ocean.   These changes were computed using the mean of

361   percentiles each region (domain, land, and ocean) for both present and future runs, and then the

362   relative changes with respect to present climate were calculated. PA suggests a decrease in all

363   selected percentiles when aggregating over the entire domain and ocean grid points. It also

364   suggests an increase in all but the 95th percentile over land. EX projects a similar behavior, except

365   for the highest one (99.9th), which increases both over land and ocean. On average, EX produces

366   larger decreases for the 95th and 98th percentiles compared to PA. This difference is strongly

367   dominated by decreases over water in EX, since changes over land are very similar between the

368   two experiments. As we move to more intense precipitation events (99th), the contrast between

369   land and ocean is further enhanced, especially for PA, which suggests substantial changes both

370   over land and ocean but with opposite signs (9.6% vs. -32.6% respectively). Indeed, some large

371   islands such as New Guinea show a strong and statistically significant response of the upper tail

372   to warming in the PA experiment (Fig. 3i).

373   The highest end of the distribution (99.9th percentile) represents events above 10 mm hr^{-1} in

374   most cases and well above 25 mm hr^{-1} in many land grid points (Supplementary Figure S3). In EX,

375   the 99.9th increases over land (14.9%) under climate change conditions, but there is no clear signal

376   over the ocean. In fact, significant changes are mostly located over land. PA shows an increase in

377   extreme precipitation (99.9th) over land (22.4%) too, but it produces significant decreases over the

378   ocean (-10.9%). As a result, PA exhibits a domain-average decrease of high-end extremes (-3.2%),

379   while EX produces an increase (4.0%).

380   Figure 3 provides a more detailed and visual description of the precipitation response to

381   warming. As opposed to the summary discussed above (Table 1), Figure 3 includes aggregated

382   information on other percentiles (50th to 100th) and shows the spatial variability of changes. Rates

383   below the 90th percentiles are usually light rainfall events (<0.1 mm hr-1) in EX (Supplementary

384   Figure S3), and their contribution to total precipitation is limited. The contribution of events below

385   the 90th percentile to total precipitation may be larger in PA, because the 0.1 mm hr^{-1} rate is reached

386   at a much lower percentile (70th). This is likely due to the drizzle effect that typically affect models

387   with convective schemes [*Gutowski et al.*, 2003; *Sun et al.*, 2006; *Dai,* 2006; *Stephens et al.,* 2010;

388   *Pendergrass and Hartmann*, 2014].

389   Moderate rainfall events (95th percentile) decrease with warming in most locations according

390   to both experiments (Fig. 3c-d). Very few grid-points show an increase of moderate precipitation

391   and they are mostly located over or near the islands. The land-sea contrast becomes increasingly

392   clear in the upper percentiles for both experiments (Fig. 3c-j). However, EX already concentrates

393   rainfall over land much more than PA under present climate conditions, thus the contrast will

394   become even sharper in EX under warming. Therefore, the spatial pattern of mean precipitation

395   changes (Fig. 2) is largely explained by changes in the high-end of the distribution, according to

396   Figure 3.

397   Overall, explicit and parameterized convection produce different precipitation distributions and

398   different precipitation changes under the same large-scale climate change signal, especially in the

399   upper tail of the distribution. Although the spatial pattern of changes is broadly similar (land-sea

400   contrast), their fine spatial detail, their magnitude, and the response of each percentile to climate

401   change is different between the two convective representations.

3.2 Thermodynamical and dynamical contributions to precipitation changes.

402

403   Our experiments suggest that the islands of the Maritime Continent will undergo higher

404   precipitation rates and more intense rainfall extremes in a warmer climate. Mechanisms that

405   produce rainfall changes are often interlaced and their contributions may act in opposite directions.

406   We quantified their combined effect by calculating changes in high percentiles of precipitation

407   and express them as a ratio with respect to the domain-average near-surface warming (*Direct*

408   method). Using near-surface temperature to estimate rainfall scaling imposes important limitations

409   because it does not consider changes in moisture availability, which often play a primary role in

410   defining precipitation extremes [*Lenderink et al.*, 2017]. Also, it assumes homogeneous warming

411   in the vertical and thus does not allow for different changes in the atmospheric water-holding

412   capacity at different vertical levels. However, it is a standard way of measuring the precipitation

413   scaling [*Westra et al.,* 2014; *Bao et al.,* 2017; *Lenderink et al.,* 2017; *Dobrinski et al.,* 2019; *Allan*

414   *et al.,* 2020] because it relies on widely available observations and model outputs. We also

415   estimated the aggregated contribution of the thermodynamical and dynamical terms of rainfall

416   scaling with temperature using the theoretical approach described in section 2.3 [*O'Gorman and*

417   *Schneider*, 2009a], and we refer to this method as *Full* scaling. The precipitation scaling was

418   decomposed into thermodynamical and dynamical terms following *Pfahl et al.* [2017]. The *direct*

419   method serves as a backdrop to test the adequacy of the theoretical approach (*full* scaling).

420   We focus on the scaling of the 99th percentile. For all methods we quantified the scaling by

421   calculating the mean of all events above the percentile for each period and each grid-point, and

422   compute the change relative to present climate values, as we have done with other precipitation

423   changes. Then, we divide it by the domain-average near-surface temperature change and estimate

424   the scaling of intense rainfall with temperature for both experiments (Fig. 4 a-d). The *direct* scaling

425 calculation shows a strong land-sea contrast of the scaling in PA. Most islands undergo increases

426 in the range 10-20% K^{-1}, while much of the ocean experience decreases, sometimes as large as -

427 20% K^{-1}. The spatial pattern of scaling is similar in EX, but the rates are not as pronounced.

428 The *full* scaling estimates (Fig. 4 c-d) yields results that compare very well with the *direct*

429 scaling calculation, including both the pattern and the magnitude of changes. Figure 4 a-d supports

430 the idea that warming leads to processes favoring more intense precipitation over land, while

431 changes of any sign are plausible over water. Ignoring changes in vertical velocities in Eq. 1 (see

432 details in section 2.3), we can estimate the separate contribution of thermodynamic (*Thermo*)

433 processes to the scaling (Fig. 4 e-f). The thermodynamic contribution to extreme precipitation

434 changes is spatially much more homogeneous than the *full* scaling, although it still presents some

435 land-sea contrast in EX. In both experiments, the thermodynamic processes contribute to increases

436 in the range 4.2-8.2% K^{-1} over virtually the entire domain (95% of grid-points), with slightly higher

437 values for EX (4.3-8.2% K^{-1}) than for PA (4.2-7.5% K^{-1}). This is roughly consistent with the

438 Clausius-Clapeyron relationship, which establishes an approximate increase in rainfall rates of 7%

439 per degree of near-surface warming [*Trenberth et al.,* 2003]. The scaling methods produce similar

440 results when using different percentiles (95th and 99.9th, see Supplementary Figures S5 and S6,

441 respectively).

442 In the results above, the vertical pressure velocity (ω_e) was smoothed using a 20-km gaussian

443 filter prior to calculating the scaling. We have also calculated the scaling without the smoothing

444 to determine the impact of this choice (Supplementary Figure S7) and found that the smoothing

445 considerably reduces the noise in both model configurations, particularly in EX. While the overall

446 pattern is similar between the two approaches, the spatial details and magnitude of the *full*

447 (theoretical) scaling is closer to the *direct* scaling when smoothing ω_e.

448   Large spatial variations in *direct* and *full* scaling estimates can only be explained by dynamic

449   processes, because the *thermo* term is spatially homogeneous. The contribution of dynamic

450   processes is calculated as the difference between the *full* scaling and the *thermo* term [*Pfahl et al.*,

451   2017]. The dynamical term enhances or opposes the effect of the thermodynamic mechanisms

452   through changes in vertical motions during extreme precipitation events. Therefore,

453   heterogeneities in vertical motions are responsible for the spatial noise in the dynamical term

454   (Supplementary Figure S8), which modulates the homogeneous thermodynamic contribution. This

455   explains the existence of positive and negative values of *direct* and *full* scaling close together.

456   Although this may be alleviated with longer runs and strengthening the gaussian spatial filter

457   applied to the vertical velocity, differences between the two experiments suggest that the nature of

458   the convective scheme may also play a role in smoothing out spatial heterogeneities of vertical

459   motions. In fact, explicit convection experiments running at few-kilometer resolutions are prone

460   to generate single-grid-cell precipitating systems [*Murata et al.,* 2017a] that may reflect into this

461   spatial noise.

462   In general, our results indicate that the dynamic term counteracts the thermodynamic effect over

463   the ocean. Over land, dynamical processes tend to enhance precipitation scaling in PA. In EX, the

464   dynamic contribution also presents a land-sea contrast, but both positive and negative contributions

465   were obtained over land. This land-sea contrast is consistent with results in *Pfahl et al.* [2017]

466   using GCMs, which suggested that dynamic processes enhanced changes in daily precipitation

467   extremes over large islands in the Maritime Continent. Differences between our two model

468   configurations are further discussed in the next section, where the vertical structure of the

469   atmosphere is analyzed.

3.3 Land-sea thermal contrasts, stability, and precipitation changes.

470

471 Our hypothesis is that warming contrasts play a key role in the spatial pattern of the

472 archipelago's rainfall response to a changing climate. Changes in moisture availability due to

473 increased atmospheric water-holding capacity and changes in the large-scale dynamics are

474 spatially too uniform to explain the fine spatial structure of precipitation changes. In the horizontal,

475 land warms faster than the ocean due to their different heat capacity, which intensifies current

476 land-sea thermal contrasts. In the vertical, changes in temperature and humidity profiles may be

477 different at each location, which affects atmospheric stability at different rates. These spatial

478 contrasts create more favorable conditions for mesoscale circulations and increased potential for

479 convective initiation. Whether this potential is realized depends on the convective representation.

480 For example, future climate change increases the land-sea thermal contrast (Fig. 5a-b) and the

481 domain-average increase is very similar in both experiments. Air over land warms faster (3.30°C

482 in both cases) than the air above the ocean (2.90°C in EX; 2.94°C in PA). Changes in thermal

483 contrast help explain precipitation changes to some extent, as we described in the previous section,

484 but differences between parameterized and explicit runs indicate that the convective representation

485 is crucial to define the rainfall response to this thermal forcing.

486 Here, we investigate the mechanism that links changes in thermal land-sea contrast and rainfall.

487 The primary source of convective potential over the islands is the moisture flux convergence at

488 the lower levels. Moisture flux convergence was calculated using:

$$MFC = -\nabla \cdot (q\mathbf{V}_h) \qquad \text{Eq. 4}$$

489 Where MFC is the moisture flux convergence, q is water vapor mixing ratio at 2m and $\mathbf{V}_h$ is the

490 horizontal wind vector at 10 m. The approach described by *Bluestein* [1992] was applied to deal

491 with discrete variables.

22

492   Because of the enhanced land-sea thermal contrast, the model produces an increase in near-

493   surface MFC along the coastlines (Fig. 5 c-d). This agrees with results in *Tangang et al.* [2020],

494   which also found an increase in low-level moisture flux convergence over the islands using

495   multiple regional climate simulations. This MFC increase on the coastline is accompanied by a

496   decrease far outside over the ocean, where negative values are observed almost everywhere. MFC

497   was decomposed into two terms (horizontal advection of specific humidity and horizontal mass

498   convergence; Eq. 5) following *Banacos and Schultz* [2005]:

$$MFC = -\boldsymbol{V}_h \cdot \nabla q - q\nabla \cdot \boldsymbol{V}_h \qquad \qquad \text{Eq. 5}$$

499   and then changes were calculated for each of them to estimate their relative contribution to

500   MFC changes. This decomposition reveals that MFC changes where largely driven by horizontal

501   convergence changes, while advection changes play a negligible role on average (Fig. 5 e-h).

502   Therefore, a higher MFC –along the coast and mostly driven by convergence changes– points

503   in the same direction as our hypothesis that mesoscale circulations (sea breeze type) intensify

504   under warmer conditions. This effect is even more marked during the time of the day when sea-

505   breeze usually builds up in the region (10-16 LST, Supplementary Figure S9). Hence, our results

506   are coherent with the idea that land-sea thermal contrasts and the resulting MFC changes are

507   drivers of rainfall redistribution and more intense precipitation over land.

508   This mechanism may be partly responsible for the intensification of rainfall over land, but there

509   must be other factors (e.g., stability) causing differences in precipitation changes between the two

510   experiments despite their very similar changes in thermal contrasts and MFC.

511   Under global warming, the upper troposphere warms faster than the lower troposphere in the

512   tropics, which increases dry static stability [*Schneider et al.,* 2010; *Chou et al.,* 2013]. We

513   estimated dry static stability in the lower troposphere from both our experiments using the

514   difference in potential temperature (θ) between the lower (850 hPa) and the middle (500 hPa)

515   troposphere. In both simulations, this difference is reduced in the future, thus indicating increased

516   dry static stability under climate change, especially for the explicit convection run (Supplementary

517   Figure S10). However, these changes in temperature are also accompanied by changes in humidity,

518   which directly affect moist adiabatic processes that govern deep convection. To incorporate this

519   factor, we analyzed changes in potential stability (also called moist static stability or convective

520   stability). Herein, we speak in terms of instability to make the interpretation of results more

521   intuitive, but it is conceptually the same. We examined the equivalent potential temperature (θ_e)

522   and its vertical profiles, which accounts for changes in both temperature and humidity. The

523   difference in θ_e between 900-800 hPa and 600-400 hPa layers provides a measure of potential

524   instability.

525   This choice is motivated by the fact that atmospheric models (e.g., CMIP5 ensemble,

526   Supplementary Figure S11) often show a discontinuity in the vertical derivative of θ_e, which is

527   likely linked to how convective processes are parameterized. The discontinuity is linked to how

528   the schemes work around the freezing level, their interaction with microphysics schemes and the

529   quasi-equilibrium profile used in certain parameterizations such as the Betts-Miller Janjic, which

530   is used in the parameterized simulations here. Indeed, this behavior is also detected in PA around

531   the 500 hPa level. This reflects on changes of the vertical profiles simply because the discontinuity

532   is shifted upwards. To reduce the dependence of our results on this issue, which we assume is a

533   model artifact, we computed potential instability using the above reference layers.

534   Vertical profiles of equivalent potential temperature (θ_e) reveal that time-mean potential

535   instability will increase everywhere under the prescribed climate change signal according to both

536   experiments (Fig. 6c). This is shown by steeper vertical profiles of θ_e under future climate

537 conditions with the largest increases in θ_e near the surface (~14-15 K). Changes over land are on

538 average very similar between PA and EX, and both show an intensification of instability in the

539 early afternoon (Fig. 6d). On the other hand, changes over the ocean are slightly larger in PA and

540 are flat throughout the day in both model runs. This spatial distribution of potential instability

541 changes is further illustrated in Figure 6 e-f, which suggest that instability will increase the most

542 over large land masses. These changes were tested for statistical significance using a Mann-

543 Whitney U test at the 99% confidence level and they are significant everywhere in the domain.

544 The land-sea contrast of potential instability changes is more pronounced in EX, mostly because

545 EX produces more moderate changes over water. If we select only days when precipitation exceeds

546 the 99.9th percentile in each grid cell and calculate the changes in potential instability, EX produces

547 much stronger changes than PA during such events (Supplementary Figure S12). Therefore,

548 despite similar time-mean changes in potential stability and mean precipitation changes, EX

549 suggest more intense extreme precipitation in a warming climate accompanied by higher potential

550 instability.

551   To understand the link between this increase in potential instability and precipitation extremes,

552 we focus on potential instability preceding events above the 99.9th percentile. To that purpose, we

553 selected 0.5° by 0.5° areas in the four largest islands (squares in Fig. 1) and calculated the area-

554 averaged potential instability (θ_e^{850hPa}-θ_e^{500hPa}) over the 12 hours before any grid cell exceeds its

555 99.9th percentile of hourly precipitation. Figure 7 shows the relationship between the intensity of

556 heavy rainfall events versus the preceding potential instability for present and future simulations,

557 both model configurations and over the four selected representative areas. Retaining only dry hours

558 to calculate convective instability as opposed to all preceding hours was tested with no substantial

559 differences (not shown) and we decided to keep the all-hour approach so that all instability values

560   were calculated using the same number of preceding hours. Different accumulation periods (6, 18,

561   24 hours) and area sizes (0.2°, 1.0°) were also tested with very similar results (not shown).

562   Different locations within each island were also examined to ensure our results were robust and

563   the outputs were qualitatively the same (Supplementary Figures S14 and S15).

564   In all cases, the atmosphere reaches a clearly different state where both potential instability and

565   extreme rainfall intensity are higher under a warmer climate. While potential instability alone is

566   not enough to determine the intensity of extreme events for each of the periods separately, this is

567   not surprising since many other factors are involved in the generation of heavy rainfall events, thus

568   the dispersion of the point clouds. However, it indicates that the model response to climate change

569   in terms of precipitation extremes and potential instability are related to each other.

570   This relationship also reveals an interesting contrast between model runs. The fully explicit

571   convection is much more dispersed in the rainfall-instability space depicted in Fig. 7. Some of the

572   differences between experiments noted before can be interpreted through this feature. For instance,

573   it shows that the convective parameterization restricts the atmospheric conditions to a given range

574   because it continuously adjusts the vertical profile towards an equilibrium state. The explicit run,

575   on the contrary, is more flexible in this sense, and it allows for higher precipitation rates

576   (Supplementary Figure S14 and S15). In fact, it also produces situations with substantially larger

577   potential instability when the extremes occur (Fig. 7). As a result, the response to climate change

578   in PA is spatially more homogeneous than in EX, which produces a noisier signal because of the

579   higher degrees of freedom explicit convection provides. Precipitation rates above the 99.9[th]

580   percentile were also compared to other variables such as potential temperature (θ), Convective

581   Available Potential Energy (CAPE) and precipitable water (PW) to illustrate their links in a

582   changing climate (Supplementary Figure S16). In agreement with our previous findings, changes

583   in the intensity of extreme rainfall are related to an increase in dry static stability (θ^{850hPa}-θ^{500hPa})

584   and an increase in latent conditional instability (CAPE). It also shows that this contrast between

585   changes in dry static stability (temperature dependent) and convective stability (temperature and

586   moisture dependent) when extremes occur is mostly due to a higher availability of precipitable

587   water, which significantly increases in the future.

588   Present and future bivariate distributions of rainfall and the various instability metrics (Fig. 7

589   and Supplementary Figures S14-S16) were tested statistically to determine if they are significantly

590   different. All present and future bivariate distributions were statistically different to each other at

591   the 0.01 significance level using a multi-dimensional version of the Kolgomorov-Smirnov (KS)

592   test [*Fassano and Franceschini,* 1987]. A classical 1-D KS test was also applied to present and

593   future precipitation distributions and were found different at the 0.01 significance level too.

594   Increased instability only produces precipitation changes if convective circulation is intensified.

595   Thus, changes in vertical motions must be considered to explain the spatial contrasts of rainfall

596   changes (see section 3.2). Here, we relate changes in vertical pressure velocity (ω_e) that precede

597   precipitation extremes with changes in the extremes themselves (Fig. 8). We binned grid points by

598   changes in extreme rainfall (total accumulated above the 99th percentile). For each bin, we

599   computed the average change in the vertical profile of ω_e over the six hours preceding each extreme

600   event. We chose a six-hour period because vertical motions due to convection start approximately

601   six hours before the peak of the precipitation diurnal cycle in the region [*Argüeso et al.* 2020].

602   On average, the atmospheric environment preceding intense rainfall is characterized by

603   ascending motions almost through the entire troposphere in both experiments and climate periods

604   (Supplementary Figures S17 and S18). Only the bottom and the top levels show small positive

605   values (descending motions). Thus, positive changes ω_e can be generally interpreted as a

606   weakening of ascending vertical motions. Both experiments concentrate stronger vertical motions

607   and rainfall extremes over land, which is consistent with the picture described in section 3.2. The

608   average ω_e preceding rainfall extremes and its changes are spatially more homogeneous in the

609   parameterized case (not shown), which is also consistent with the results above (Fig. 7 and

610   Supplementary Figures S14-S16).

611   Not only rainfall extremes are collocated with more intense upward motions, but also their

612   changes. Areas where rainfall extremes will increase the most coincide with stronger upward

613   motions, particularly above 800hPa (red in Fig.8). Likewise, extreme rainfall decreases are

614   accompanied by weakened ascending winds (blue in Fig. 8). Weakened vertical motions (blue)

615   extend across the zero-change line, hence small increases (<20%) in extreme precipitation occur

616   with decreases in vertical rising motions, especially over land and when convection is explicit (Fig.

617   8f). It is likely that changes in ω_e partly offset the effect of warming, but the latter still dominates

618   in this range. These results are consistent with the decomposition of scaling in dynamical and

619   thermodynamical terms, where vertical motions help explain spatial contrasts in extreme rainfall

620   changes. Similar results were obtained for other percentiles too (95th and 99.9th; not shown).

621   Most ocean areas show a decrease in precipitation extremes (99th percentile; Fig. 3g-h and Fig

622   8c-d) and weakening of vertical motions preceding such intense rainfall events (Fig. 8c-d). On the

623   other hand, upward vertical velocity before extreme events tend to intensify where heavy rainfall

624   increases over the ocean.

625   This aggregated view reveals some similarities and differences between the two convective

626   representations. Both runs expand the range of possible extremes to higher values, especially EX

627   (Supplementary Figures S17-S18). They also tend to increase the land-sea contrast of ω_e under a

628   warmer climate, particularly PA, as shown the intensification of blue areas in Fig 8c and read areas

629 in Fig 8e. As for the differences, PA tends to produce larger changes in vertical motions (Fig. 8),

630 and they are spatially more organized and uniform in the vertical (not shown). In the explicit

631 convection run, most changes of extreme precipitation over land lie around 20% (Fig. 8f, top) and

632 vertical motions are weakened in the lower-to-middle troposphere for this range of precipitation

633 and intensified in the atmosphere above. This feature can be interpreted as a deepening of the

634 convective circulation and expansion of the convective cell upwards. *Argüeso et al.* [2020] also

635 found that EX produces deeper convective circulations than PA under present climate condition,

636 a difference that could be enhanced with warming.

637 Therefore, the importance of land masses in the convective development and their role as

638 rainfall attractor in the two model experiments is different. The concentration of rainfall over land

639 seems to strengthen under future climate conditions as the land-sea thermal contrast intensifies and

640 the potential instability increases, because they favor moisture convergence and convective

641 circulations over the islands. However, the model responds differently to these changes depending

642 on how convection is represented, especially in terms of vertical pressure velocity. The need for

643 triggering factors in the explicit case and the constrains imposed by the deep parameterization

644 scheme may help explain these differences in vertical motions and precipitation intensities.

4   Conclusions

646 We studied the role of horizontal and vertical warming contrasts on precipitation changes in the

647 Maritime Continent for the late 21st century under a RCP8.5 scenario using a Pseudo-Global

648 Warming approach. We analyzed results from a regional climate model operating at convection-

649 permitting scales with two different representations of deep convection: parameterized and

650 explicit.

651   We found that the model produces a domain-averaged decrease of rainfall during the Maritime

652   Continent wet season (NDJF) for both convective representations, although there is a marked land-

653   ocean contrast. Both model configurations tend to produce a decrease over the ocean and an

654   increase over land. Even though GCMs do not agree on the sign of rainfall changes for the region,

655   their spatial pattern of changes is consistent with the land-ocean contrast we obtained [*Jourdain et*

656   *al.,* 2013; *Wang et al.,* 2020]. The ensemble mean of GCMs selected in this study projects a

657   domain-average increase in rainfall and in the vertically integrated water vapor. Thus, the decline

658   of domain-average precipitation suggested by our model experiments cannot be explained by

659   changes in the large-scale water vapor supply (i.e., advection). Instead, it must be explained by

660   processes that transform the available water vapor into precipitation and how they are represented

661   in models.

662   Our experiments suggest that the islands of the Maritime Continent will undergo more intense

663   mean and extreme precipitation in a warmer climate. However, extremes behave differently under

664   the same large-scale climate change signal depending on how convection is represented. This

665   includes their magnitude, spatial pattern, and the relative changes of the various percentiles. The

666   most prominent difference is that the land-sea contrast of changes is more pronounced in the

667   parameterized runs. The upper percentiles of rainfall undergo larger increases relative to present

668   climate extremes when convection is parameterized. However, explicit convection expands the

669   range of possible future extremes to higher values. This is partly because present climate extremes

670   in EX are already more intense than in PA, but also because the convective scheme constrains the

671   response to warming. Therefore, future generations of climate projections at convection-permitting

672   resolutions may project different outlooks for rainfall extremes to those currently available.

673   We determined the contribution of thermodynamical and dynamical processes to changes in

674   rainfall extremes under a warmer climate. Thermodynamic effects account for changes in

675   precipitation extremes that are consistent with the Clausius-Clapeyron relationship, and their

676   contribution is relatively homogeneous across the domain. Thus, we need to invoke dynamical

677   processes to explain features of extreme rainfall changes, such as their magnitude range (-20% K$^-$

678   ^{1} to 20% K^{-1}), their spatial contrasts and the divergences between the two model runs.

679   According to our simulations, the primary driver of changes in the spatial distribution of rainfall

680   is the land-sea thermal contrast and its enhancement under climate change. Land warms faster than

681   the ocean, which favors local sea-breeze type circulations. These circulations increase low-level

682   moisture flux convergence over land and contribute to create conditions for deep convection

683   development over land. They are also responsible for suppressing rainfall generation over the

684   ocean to some extent.

685   Deep convection and heavy rainfall require atmospheric instability to occur. Climate change

686   modifies the vertical profile of the atmosphere and thus alters the overall stability. Although dry

687   static stability increases under future climate conditions because the upper half of the troposphere

688   warms faster, the combined effect of temperature and humidity changes in the vertical makes the

689   atmosphere more unstable in terms of moist static stability. While both model experiments show

690   this response to climate change, the convective scheme constrains potential instability and extreme

691   precipitation values within a narrower range. Under future climate conditions, this means the

692   model with explicit convection allows heavier rainfall events to occur. Yet, changes relative to

693   present climate values are higher in the parameterized case. Also, the convective scheme produces

694   a response to climate change that is spatially more uniform, while explicit convection generates

695   noisier patterns of extreme precipitation changes.

696 Deep convection entails intense upward vertical motions. Thus, extreme precipitation is linked

697 to high vertical pressure velocity. We found that the model tends to concentrate strong vertical

698 motions and rainfall extremes over land, especially when convection is explicitly resolved. In some

699 land areas, this is enhanced in future climate simulations, which explains departures from the

700 thermodynamic contribution to extreme rainfall changes. Changes in vertical winds also indicate

701 a possible expansion of the convective cell over the islands and a slight weakening of upward

702 motions in the mid troposphere. Even though explicit convection produces more extreme rainfall

703 events over land in the future —due to further concentration of upward motions over large islands

704 and the lack of convective scheme constrains—, the parameterized case suggests stronger changes

705 relative to present climate values. In fact, the model produces stronger changes in vertical motions

706 preceding extreme events with climate change when convection is parameterized. This refers not

707 only to the strengthening of vertical winds over land, but also to their weakening over the ocean.

708 In both model configurations, areas of stronger upward vertical pressure velocity are collocated

709 with positive changes in extreme precipitation, and vice versa. This spatial coincidence, together

710 with the scaling decomposition into thermodynamical and dynamical terms, evidences the role of

711 vertical motions in modulating the intensity of future climate rainfall events.

712 In summary, we showed that the way convection is represented is crucial in defining the model

713 response to warming, because it defines dynamical processes that shape the future distribution of

714 precipitation and the intensity of extremes.

715 ## Acknowledgements

739

740   **Data availability statement**

741   The data on which this paper is based is too large (~ 120TB) to be publicly archived with

742   available resources. The model version used in this study is open source and publicly available

743   (https://github.com/NCAR/WRFV3/releases). Sample namelists to reproduce the experiments are

744   archived and available in a public repository (10.5281/zenodo.4624353). All retained data is

745   available upon request addressed to Daniel Argüeso (d.argueso@uib.es).

746   **References**

747   Argüeso, D., A. Di Luca, and J. P. Evans (2016), Precipitation over urban areas in the western

748   Maritime Continent using a convection-permitting model, *Clim. Dyn.*, *47*(3), 1143–1159,

749   doi:10.1007/s00382-015-2893-6.

750   Argüeso, D., R. Romero, and V. Homar (2020), Precipitation Features of the Maritime

751   Continent in Parameterized and Explicit Convection Models, *J. Climate*, *33*(6), 2449–2466,

752   doi:10.1175/JCLI-D-19-0416.1.

753   Banacos, P. C., and D. M. Schultz (2005), The use of moisture flux convergence in forecasting

754   convective initiation: Historical and operational perspectives, *Wea. Forecasting*, *20*(3), 351–366,

755   doi:10.1175/WAF858.1.

756   Baranowski, D. B., D. E. Waliser, X. Jiang, J. A. Ridout, and M. K. Flatau (2019),

757   Contemporary GCM Fidelity in Representing the Diurnal Cycle of Precipitation Over the Maritime

758   Continent, *J. Geophys. Res. Atmos.*, *124*(2), 747–769, doi:10.1029/2018JD029474.

759   Birch, C. E., M. J. Roberts, L. Garcia-Carreras, D. Ackerley, M. J. Reeder, A. P. Lock, and R.

760   Schiemann (2015), Sea-Breeze Dynamics and Convection Initiation: The Influence of Convective

761   Parameterization in Weather and Climate Model Biases, *J. Climate*, *28*(20), 8093–8108,

762   doi:10.1175/JCLI-D-14-00850.1.

763   Birch, C. E., S. Webster, S. C. Peatman, D. J. Parker, A. J. Matthews, Y. Li, and M. E. E.

764   Hassim (2016), Scale Interactions between the MJO and the Western Maritime Continent, *J.*

765   *Climate*, *29*(7), 2471–2492, doi:10.1175/JCLI-D-15-0557.1.

766   Bony, S., G. Bellon, D. Klocke, S. Sherwood, S. Fermepin, and S. Denvil (2013), Robust direct

767   effect of carbon dioxide on tropical circulation and regional precipitation, *Nature Geoscience*, *6*(6),

768   447–451, doi:10.1038/ngeo1799.

769   Cai, W., G. Wang, B. Dewitte, L. Wu, A. Santoso, K. Takahashi, Y. Yang, A. Carréric, and M.

770   J. McPhaden (2018), Increased variability of eastern Pacific El Niño under greenhouse warming,

771   *Nature*, 564(7735), 201–206, doi:10.1038/s41586-018-0776-9.

772   Chan, S. C., E. J. Kendon, N. M. Roberts, H. J. Fowler, and S. Blenkinsop (2016), Downturn

773   in scaling of UK extreme rainfall with temperature for future hottest days. *Nature Geoscience*, 9,

774   24–28, https://doi.org/10.1038/ngeo2596.

775   Chen, J., Z. Wang, C.-Y. Tam, N.-C. Lau, D.-S. D. Lau, and H.-Y. Mok (2020), Impacts of

776   climate change on tropical cyclones and induced storm surges in the pearl River Delta region using

777   pseudo-global- warming method, *Sci. Rep.*, 1–10, doi:10.1038/s41598-020-58824-8.

778   Chou, C., Chiang, J. C. H., Lan, C. W., Chung, C. H., Liao, Y. C., & Lee, C. J. (2013). Increase

779   in the range between wet and dry season precipitation. *Nature Geoscience*, 6(4), 263–267.

780   https://doi.org/10.1038/ngeo1744

781   Contractor, S., M.G. Donat, and L.V. Alexander (2018), Intensification of the Daily Wet Day

782   Rainall Distribution Across Australia, *Geophys. Res. Lett.*, 45, 8568-8576, doi:

783   10.1029/2018GL078875

784   Contractor, S., M.G. Donat, and L.V. Alexander (2021), Changes in Observed Daily

785   Precipitation over Global Land Areas since 1950, *J. Climate*, 34(1), 3-19, doi: 10.1175/JCLI-D-

786   19-0965.1

787   Dai, A. (2006), Precipitation characteristics in eighteen coupled climate models, *J. Climate*,

788   19(18), 4605-4630, doi: 10.1175/JCLI3884.1

789   Donat-Magnin, M., N. C. Jourdain, C. Kittel, C. Agosta, C. Amory, H. Gallée, G. Krinner, and

790   M. Chekki (2021), Future surface mass balance and surface melt in the Amundsen sector of the

791   West Antarctic Ice Sheet, *The Cryosphere*, 15, 571–593, doi:10.5194/tc-15-571-2021.

792   Drobinski, P. et al. (2018), Scaling precipitation extremes with temperature in the

793   Mediterranean: past climate assessment and projection in anthropogenic scenarios, *Clim. Dyn.*,

794   51(3), 1237–1257, doi:10.1007/s00382-016-3083-x.

795   Dutheil, C., M. Lengaigne, M. Bador, J. Vialard, J. Lefèvre, N. Jourdain, S. Jullien, A. Peltier,

796   B. Sultan, and C. Menkès (2020), Impact of projected sea surface temperature biases on tropical

797   cyclones projections in the South Pacific, *Sci. Rep.*, 1–12, doi:10.1038/s41598-020-61570-6.

798   Fasano, G., and A. Franceschini (1987), A multidimensional version of the Kolmogorov-

799   Smirnov test. *Mon. Not. R. Astr. Soc.*, 225, 155-170, doi: 10.1093/mnras/225.1.155.

800   Fiedler, S. et al. (2020), Simulated Tropical Precipitation Assessed across Three Major Phases

801   of the Coupled Model Intercomparison Project (CMIP), *Mon. Wea. Rev.*, *148*(9), 3653–3680,

802   doi:10.1175/MWR-D-19-0404.1.

803   Fosser, G., E. J. Kendon, D. Stephenson, and S. Tucker (2020), Convection- Permitting Models

804   Offer Promise of More Certain Extreme Rainfall Projections, *Geophys. Res. Lett.*, *47*(13), 1–9,

805   doi:10.1029/2020GL088151.

806   Gutowski Jr., W., Decker, S., Donavon, R., Pan, Z., Arritt, R., and Takle, E (2003), Temporal-

807   spatial scales of observed and simulated precipitation in central U.S. climate, *J. Climate*, 16, 3841–

808   3847, doi: 10.1175/1520-0442(2003)016%3C3841:TSOOAS%3E2.0.CO;2

809   Hassim, M. E. E., T. P. Lane, and W. W. Grabowski (2016), The diurnal cycle of rainfall over

810   New Guinea in convection-permitting WRF simulations, *Atmos. Chem. Phys.*, 16(1), 161–175,

811   doi:10.5194/acp-16-161-2016.

812   Held, I. M., and B. J. Soden (2006), Robust responses of the hydrological cycle to global

813   warming, *J. Climate*, 19(21), 5686–5699, doi:10.1175/JCLI3990.1.

814   Hersbach, H., Bell, B., Berrisford, P., Hirahara, S., Horányi, A., Muñoz- Sabater, J., and others

815   (2020). The ERA5 global reanalysis. *Q.J.R. Meteorol. Soc*, 146(730), 1999-2049, doi:

816   10.1002/qj.3803.

817   Hong, S. Y., and J. Lim (2006), The WRF single-moment 6-class microphysics scheme

818   (WSM6), *J Korean Meteor Soc*, 42(2), 129–151.

819   Im, E. S., and E. Elthair (2018), Simulation of the diurnal variation of rainfall over the western

820   Maritime Continent using a regional climate model, *Clim. Dyn.*, 51(1-2), 73–88,

821   doi:10.1007/s00382-017-3907-3.

822   IPCC, 2013: Annex I: Atlas of Global and Regional Climate Projections Supplementary

823   Material RCP8.5 [van Oldenborgh, G.J., M. Collins, J. Arblaster, J.H. Christensen, J. Marotzke,

824   S.B. Power, M. Rummukainen and T. Zhou (eds.)]. In: Climate Change 2013: The Physical

825   Science Basis. Contribution of Working Group I to the Fifth Assessment Report of the

826   Intergovernmental Panel on Climate Change [Stocker, T.F., D. Qin, G.-K. Plattner, M. Tignor,

827   S.K. Allen, J. Boschung, A. Nauels, Y. Xia, V. Bex and P.M. Midgley (eds.)]. Available from

828   www.climatechange2013.org and www.ipcc.ch.

829   Joshi, M. M., J. M. Gregory, M. J. Webb, D. M. H. Sexton, and T. C. Johns (2007), Mechanisms

830   for the land/sea warming contrast exhibited by simulations of climate change, *Clim. Dyn.*, *30*(5),

831   455–465, doi:10.1007/s00382-007-0306-1.

832   Jourdain, N.C, A. Sen Gupta, A.S. Taschetto, C.C. Ummenhofer, A.F. Moise and K. Ashok

833   (2013), The Indo-Australian monsoon and its relationship to ENSO and IOD in reanalysis data and

834   the CMIP3/CMIP5 simulations, *Clim. Dyn.*, 41, 3073–3102, doi: 10.1007/s00382-013-1676-1.

835   Knutti, R., R. Furrer, C. Tebaldi, J. Cermak, and G. A. Meehl (2010), Challenges in Combining

836   Projections from Multiple Climate Models, *J. Climate*, *23*(10), 2739–2758,

837   doi:10.1175/2009JCLI3361.1.

838   Krinner, G., and M. G. Flanner (2018), Striking stationarity of large-scale climate model bias

839   patterns under strong climate change, *PNAS*, *115*(38), 9462–9466, doi:10.1073/pnas.1807912115.

840   Lambert, F. H., A. J. Ferraro, and R. Chadwick (2017), Land–Ocean Shifts in Tropical

841   Precipitation Linked to Surface Temperature and Humidity Change, *J. Climate*, *30*(12), 4527–

842   4545, doi:10.1175/JCLI-D-16-0649.1.

843   Li, Y., A. Sen Gupta, A. S. Taschetto, N. C. Jourdain, A. Di Luca, J. M. Done, and J.-J. Luo

844   (2020), Assessing the role of the ocean–atmosphere coupling frequency in the western Maritime

845   Continent rainfall, *Clim. Dyn.*, *54*(11), 4935–4952, doi:10.1007/s00382-020-05266-7.

846   Li, Y., N. C. Jourdain, A. S. Taschetto, A. Sen Gupta, D. Argüeso, S. Masson, and W. Cai

847   (2016), Resolution dependence of the simulated precipitation and diurnal cycle over the Maritime

848   Continent, *Clim. Dyn.*, *48*(11-12), 1–20, doi:10.1007/s00382-016-3317-y.

849   Ling, J., C. Zhang, R. Joyce, P. P. Xie, and G. Chen (2019), Possible Role of the Diurnal Cycle

850   in Land Convection in the Barrier Effect on the MJO by the Maritime Continent, *Geophys. Res.*

851   *Lett.*, *46*(5), 3001–3011, doi:10.1029/2019GL081962.

852   Lucas-Picher, P., D. Argüeso, E. Brisson, Y. Tremblay, P. Berg, A. Lemonsu, S. Kotlarski and

853   C. Caillaud (2021) Convection-permitting modelling with regional climate models: latest

854   developments and next steps. WIREs Climate Change, 12(6): e731, doi: 10.1002/wcc.731

855   Narsey, S. Y., J. R. Brown, R. A. Colman, F. Delage, S. B. Power, A. F. Moise, and H. Zhang

856   (2020), Climate Change Projections for the Australian Monsoon from CMIP6 Models, *Geophys.*

857   *Res. Lett.*, *47*(13), 147–9, doi:10.1029/2019GL086816.

858   Neale, R., and J. Slingo (2003), The maritime continent and its role in the global climate: A

859   GCM study, *J. Climate*, *16*(5), 834–848, doi:10.1175/1520-

860   0442(2003)016<0834:TMCAIR>2.0.CO;2.

861   O'Gorman, P. A., and T. Schneider (2009a), Scaling of Precipitation Extremes over a Wide

862   Range of Climates Simulated with an Idealized GCM, *J. Climate*, *22*(21), 5676–5685,

863   doi:10.1175/2009JCLI2701.1.

864   O'Gorman, P. A., and T. Schneider (2009b), The physical basis for increases in precipitation

865   extremes in simulations of 21st-century climate change, *PNAS*, *106*(35), 14773–14777,

866   doi:10.1073/pnas.0907610106.

867   Peatman, S. C., A. J. Matthews, and D. P. Stevens (2014), Propagation of the Madden-Julian

868   Oscillation through the Maritime Continent and scale interaction with the diurnal cycle of

869   precipitation, *Q.J.R. Meteorol. Soc.*, *140*(680), 814–825, doi:10.1002/qj.2161.

870   Pendergrass, A.G., and D.L. Hartmann (2014), Two modes of change of the distribution of rain,

871   *J. Climate*, 27(22), 8357-8371, doi: 10.1175/JCLI-D-14-00182.1.

872   Pfahl, S., P. A. O'Gorman, and E. M. Fischer (2017), Understanding the regional pattern of

873   projected future changes in extreme precipitation, *Nat Clim Change*, *7*(6), 423–427,

874   doi:10.1038/nclimate3287.

875   Prein, A. F. et al. (2015), A review on regional convection-permitting climate modeling: Demonstrations, prospects, and challenges, *Rev Geophys*, *53*(2), 323–361, doi:10.1002/2014RG000475.

878   Prein, A. F., R. Rasmussen, C. L. Castro, A. Dai, and J. Minder (2020), Special issue: Advances in convection-permitting climate modeling, *Clim. Dyn.*, *55*(1), 1–2, doi:10.1007/s00382-020-05240-3.

881   Qian, J.-H. (2008), Why Precipitation Is Mostly Concentrated over Islands in the Maritime Continent, *J. Atmos. Sci.*, *65*(4), 1428–1441, doi:10.1175/2007JAS2422.1.

883   Qian, J.-H., A. W. Robertson, and V. Moron (2010), Interactions among ENSO, the Monsoon, and Diurnal Cycle in Rainfall Variability over Java, Indonesia, *J. Atmos. Sci.*, *67*(11), 3509–3524, doi:10.1175/2010JAS3348.1.

886   Ruppert, J. H., and F. Zhang (2019), Diurnal forcing and phase locking of gravity waves in the maritime continent, *J. Atmos. Sci.*, *76*(9), 2815–2835, doi:10.1175/JAS-D-19-0061.1.

888   Ruppert, J. H., Jr., and X. Chen (2020), Island Rainfall Enhancement in the Maritime Continent, *Geophys. Res. Lett.*, *47*(5), 1–9, doi:10.1029/2019GL086545.

890   Schär, C., C. Frei, D. Lüthi, and H. C. Davies (1996), Surrogate climate-change scenarios for regional climate models, *Geophys. Res. Lett.*, *23*(6), 669–672, doi:10.1029/96GL00265.

892   Schär, C. et al. (2016), Percentile indices for assessing changes in heavy precipitation events, *Climatic Change*, *137*(1-2), 201–216, doi:10.1007/s10584-016-1669-2.

894   Schiemann, R., M. E. Demory, M. S. Mizielinski, M. J. Roberts, L. C. Shaffrey, J. Strachan, and P. L. Vidale (2013), The sensitivity of the tropical circulation and Maritime Continent precipitation to climate model resolution, *Clim. Dyn.*, *42*(9-10), 2455–2468, doi:10.1007/s00382-013-1997-0.

898   Schneider, T., P. A. O'Gorman, and X. Levine (2010), Water vapor and the dynamics of climate

899   changes, *Rev. Geophys.*, 48, RG3001. doi:10.1029/2009RG000302.

900   Seneviratne, S. I., X. Zhang, M. Adnan, W. Badi, C. Dereczynski, A. Di Luca, S. Ghosh, I.

901   Iskandar, J. Kossin, S. Lewis, F. Otto, I. Pinto, M. Satoh, S. M. Vicente-Serrano, M. Wehner, B.

902   Zhou, 2021, Weather and Climate Extreme Events in a Changing Climate. In: Climate Change

903   2021: The Physical Science Basis. Contribution of Working Group I to the Sixth Assessment

904   Report of the Intergovernmental Panel on Climate Change [Masson-Delmotte, V., P. Zhai, A.

905   Pirani, S. L. Connors, C. Péan, S. Berger, N. Caud, Y. Chen, L. Goldfarb, M. I. Gomis, M. Huang,

906   K. Leitzell, E. Lonnoy, J. B. R. Matthews, T. K. Maycock, T. Waterfield, O. Yelekçi, R. Yu and

907   B. Zhou (eds.)]. Cambridge University Press. In Press.

908   Seth, A., A. Giannini, M. Rojas, S.A. Rauscher, S. Bordoni, D. Singh, and S.J. Camargo (2019)

909   Monsoon Responses to Climate Changes—Connecting Past, Present and Future. *Curr. Clim.*

910   *Change Rep.,* 5, 63–79. doi:10.1007/s40641-019-00125-y

911   Skamarock, W. C., J. B. Klemp, J. Dudhia, D. O. Gill, D. M. barker, M. G. Duda, X.-Y. Huang,

912   W. Wang, and J. G. Powers (2008), A Description of the Advanced Research WRF Version 3,

913   *NCAR/TN-475+STR NCAR TECHNICAL NOTE*, 125.

914   Stephens, G. L., T. L'Ecuyer, R. Forbes, A. Gettlemen, J.- C. Golaz, A. Bodas- Salcedo, K.

915   Suzuki, P. Gabriel, and J. Haynes (2010), Dreary state of precipitation in global models, *J.*

916   *Geophys. Res.*, 115, D24211, doi:10.1029/2010JD014532.

917   Sun, Y., Solomon, S., Dai, A., & Portmann, R. W. (2006). How often does it rain? *J. Climate*,

918   19, 916–934. https://doi.org/10.1175/ JCLI3672.1.1996

919   Supari et al. (2020), Multi-model projections of precipitation extremes in Southeast Asia based

920   on CORDEX-Southeast Asia simulations, *Environmental Research*, *184*, 109350,

921   doi:10.1016/j.envres.2020.109350.

922   Tangang, F. et al. (2020), Projected future changes in rainfall in Southeast Asia based on

923   CORDEX–SEA multi-model simulations, *Clim. Dyn.*, *55*(5), 1247–1267, doi:10.1007/s00382-

924   020-05322-2.

925   Trenberth, K. E. (1999), Conceptual framework for changes of extremes of the hydrological

926   cycle with climate change, *Climatic Change*, *42*(1), 327–339, doi:10.1023/A:1005488920935.

927   Trenberth, K. E., A. Dai, R.M. Rasmussen, and D.B. Parsons, The changing character of

928   precipitation, *Bull. Am. Meteorol. Soc.* 84, 1205-1217, doi: 10.1175/BAMS-84-9-1205.

929   Vincent, C. L., and T. P. Lane (2017), A 10-Year Austral Summer Climatology of Observed

930   and Modeled Intraseasonal, Mesoscale, and Diurnal Variations over the Maritime Continent, *J.*

931   *Climate*, *30*(10), 3807–3828, doi:10.1175/JCLI-D-16-0688.1.

932   Vincent, C. L., and T. P. Lane (2018), Mesoscale Variation in Diabatic Heating around Sumatra,

933   and Its Modulation with the Madden–Julian Oscillation, *Mon. Wea. Rev.*, *146*(8), 2599–2614,

934   doi:10.1175/MWR-D-17-0392.1.

935   Wang, B., C. Jin, and J. Liu (2020), Understanding Future Change of Global Monsoons

936   Projected by CMIP6 Models, *J. Climate*, *33*(15), 6471–6489, doi:10.1175/JCLI-D-19-0993.1.

937   Wei, Y., Z. Pu, and C. Zhang (2020), Diurnal Cycle of Precipitation Over the Maritime

938   Continent Under Modulation of MJO: Perspectives from Cloud- Permitting Scale Simulations, *J.*

939   *Geophys. Res. Atmos.*, *125*(13), 2019–28, doi:10.1029/2020JD032529.

940   Yamanaka, M. D., S.-Y. Ogino, P.-M. Wu, H. Jun-Ichi, S. Mori, J. Matsumoto, and F.

941   Syamsudin (2018), Maritime continent coastlines controlling Earth's climate, *Prog Earth Planet*

942   *Sci*, *5*(1), 1–28, doi:10.1186/s40645-018-0174-9.

943   Yang, S., T. Zhang, Z. Li, and S. Dong (2020), Climate Variability over the Maritime Continent

944   and Its Role in Global Climate Variation: A Review, *J Meteorol Res*, *33*(6), 993–1015,

945   doi:10.1007/s13351-019-9025-x.

946   Yim, B. Y., S.-W. Yeh, H.-J. Song, D. Dommenget, and B. J. Sohn (2017), Land-sea thermal

947   contrast determines the trend of Walker circulation simulated in atmospheric general circulation

948   models, *Geophys. Res. Lett.*, *44*(11), 5854–5862, doi:10.1002/2017GL073778.

949   Yoshikane, T., F. Kimura, H. Kawase, and T. Nozawa (2012), Verification of the Performance

950   of the Pseudo-Global-Warming Method for Future Climate Changes during June in East Asia,

951   *SOLA*, *8*(0), 133–136, doi:10.2151/sola.2012-033.

952

953

954

955

956

957

958

959

960

961

962 **Table 1:** Domain-average changes in mean precipitation and the upper percentiles of hourly

963 rainfall for the parameterized (PA) and explicit (EX) convection experiments. Changes for all

964 grid points, land-only grid points and ocean-only grid points. Changes are in percentage with

965 respect to present climate and positive changes are in bold typeface.

		Mean	95th	98th	99th	99.9th
PA	Total	-13.3	-9.8	-14.4	-19.2	-3.2
	Ocean	-20.2	-11.8	-22.0	-32.6	-10.9
	Land	**4.3**	-5.3	**1.5**	**9.6**	**22.4**
EX	Total	-6.2	-18.9	-17.3	-12.8	**4.0**
	Ocean	-12.7	-47.1	-33.4	-23.7	**0.6**
	Land	**5.0**	-5.3	**0.6**	**5.4**	**14.9**

966

967

968
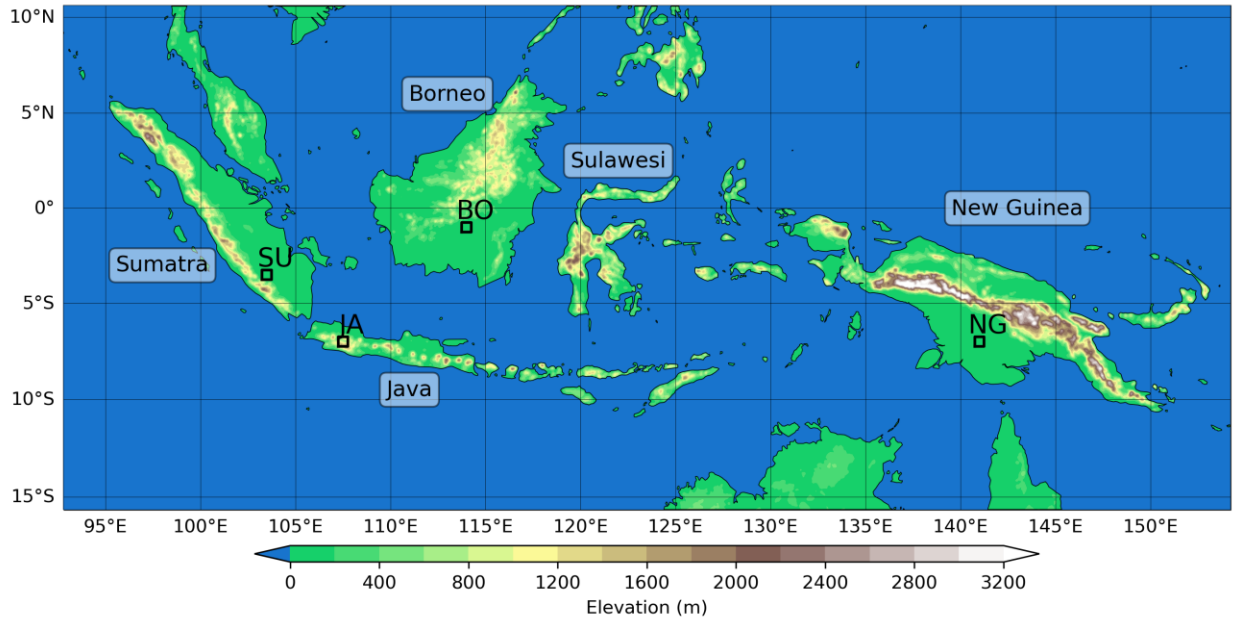
Figure 1: The Maritime Continent archipelago. The region shown corresponds to the model domain and the black squares are sampling areas.

971

972
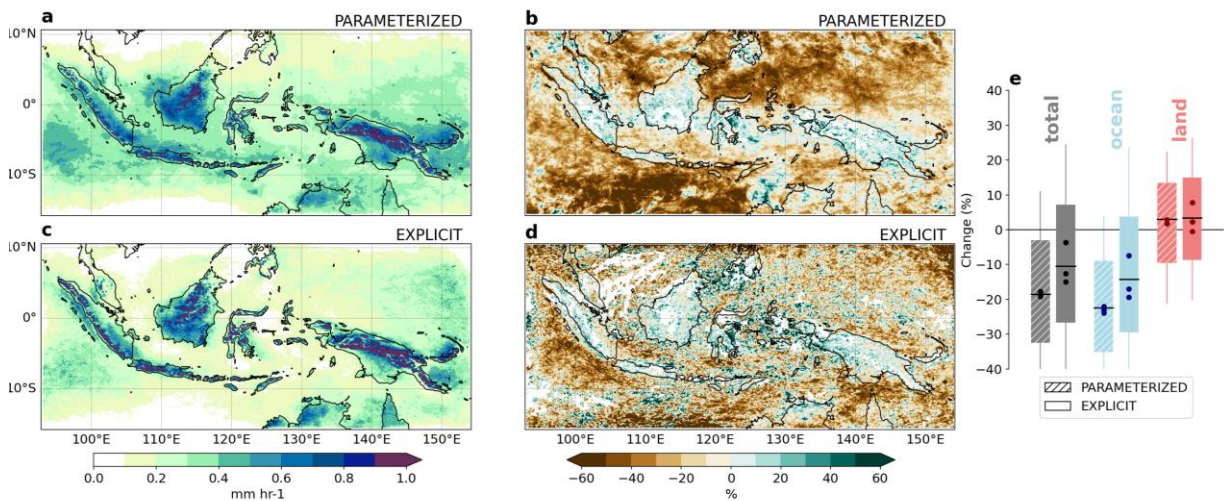
Figure 2: Present mean precipitation rates in the parameterized (a) and the explicit convection runs (c). Relative mean precipitation changes using PGW approach (future minus present) for parameterized (b) and explicit (d) convection runs. Areas with no statistically significant changes

976   according to a Mann-Whitney U test at the 99% confidence level are masked out in (b) and (d).

977   These areas are 7.9% and 14.7% of the domain, respectively. Boxplots show changes for all (gray),

978   ocean-only (blue) and land-only (red) grid cells for parameterized (hatched) and explicit (solid)

979   experiments. The boxes represent the interquartile range, whiskers are the 10th-90th percentile

980   range, horizontal lines are the median changes over all grid points in each category, and markers

981   show the median for each of the 4-month periods individually.

982

983
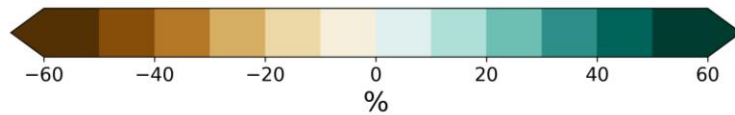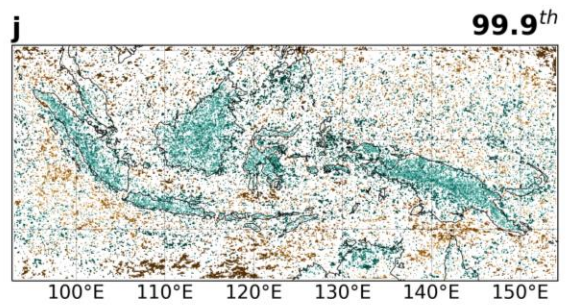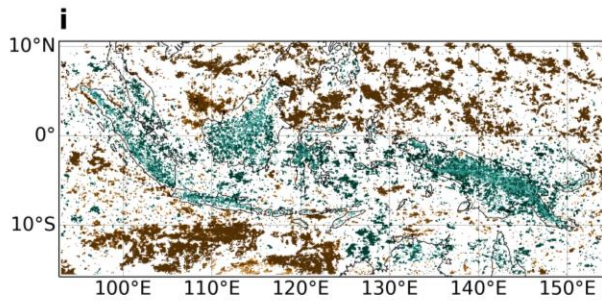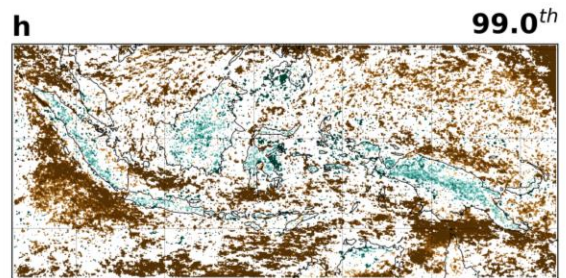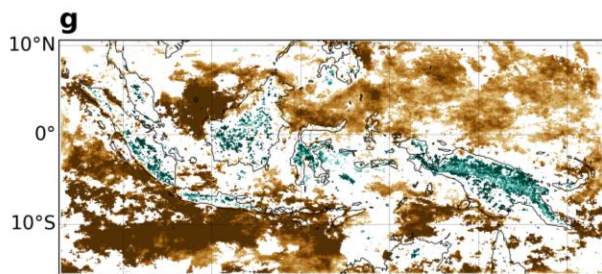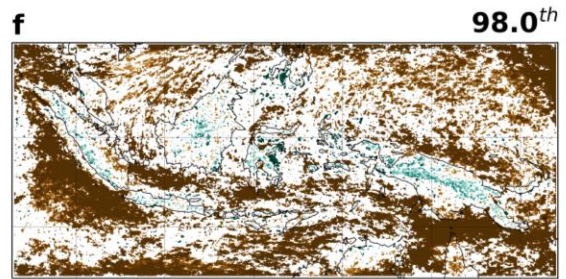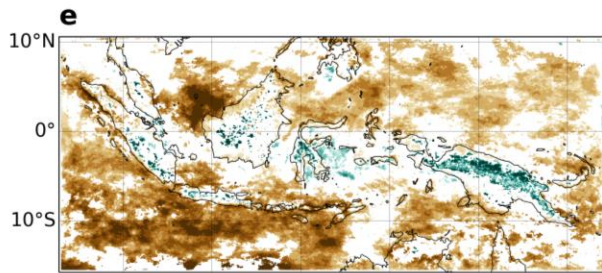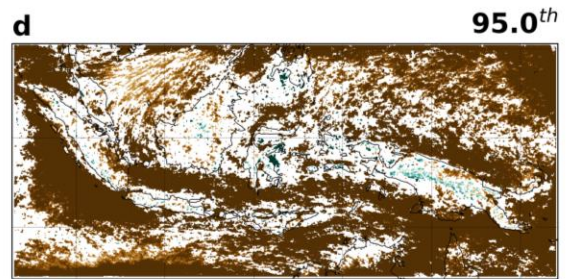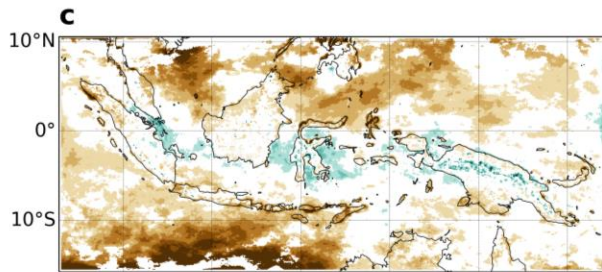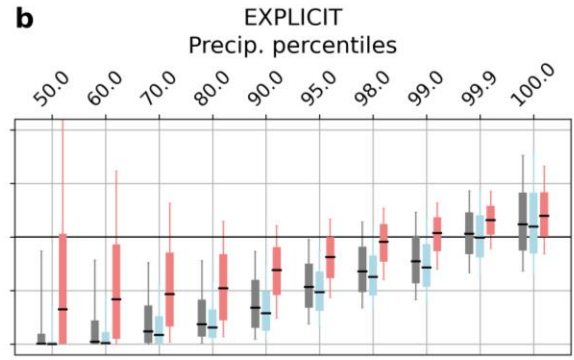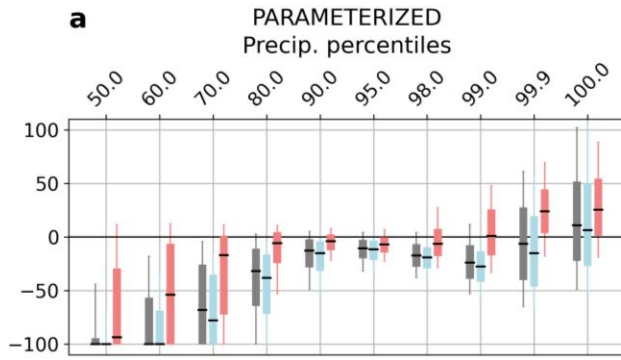
984   **Figure 3:** Changes in rainfall percentiles. Statistics of changes over the entire domain (gray),

985   ocean-only (blue) and land-only (red) grid points for the parameterized (a) and the explicit case

986   (b). Boxes represent the interquartile range; whiskers are the 10th-90th percentile range and

987   horizontal lines are the medians. Spatial patterns of relative changes in rainfall for the 95th (c, d),

988   98th (e, f), 99th (g, h) and 99.9^{th} (i, j) percentiles for the parameterized (left column) and explicit

989   (right column) model setups. Statistical significance was tested using a bootstrap approach based

990   on 12-hour blocks resampling with replacement repeated 1000 times. According to the test, 43.2%,

991   46.7%, 42.1% and 19.5% of all the grid-points show significant changes for the corresponding

992   percentiles in the parameterized runs, and 52,2%, 35.3%, 25.8% and 13.1% for the explicit case.

993   Non-significant changes were masked out.

994
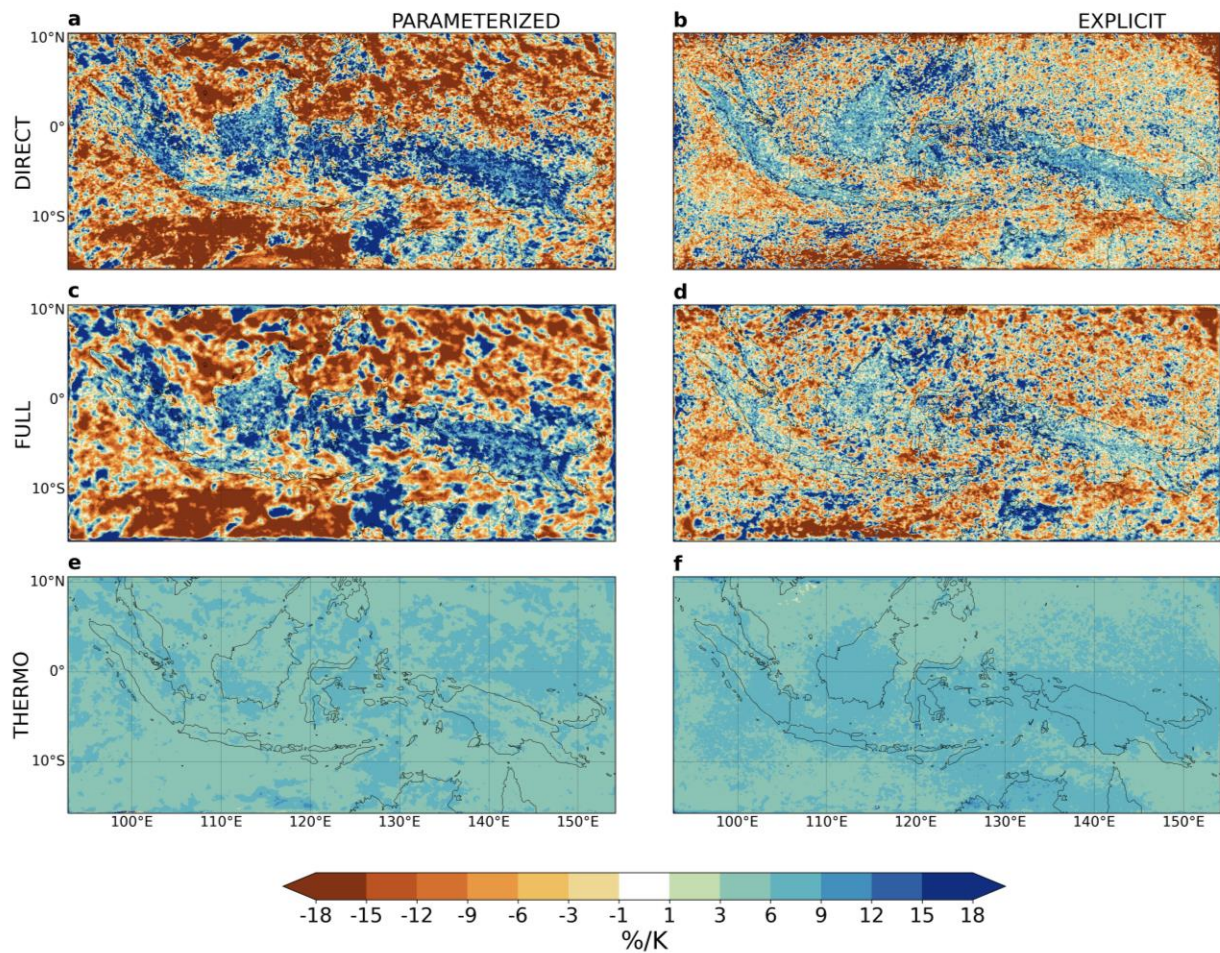
Figure 4: Scaling of the 99th percentile of precipitation with respect to the domain-average 2-m temperature change using hourly precipitation outputs from the model (*direct* scaling; a, b), the full scaling as estimated by the theoretical diagnostic from O'Gorman and Schenider [2009b] (c, d) and the thermodynamic scaling as approximated by Pfahl et al. [2017] (e, f). Left column is for the parameterized experiment and right column is for the explicit simulation.
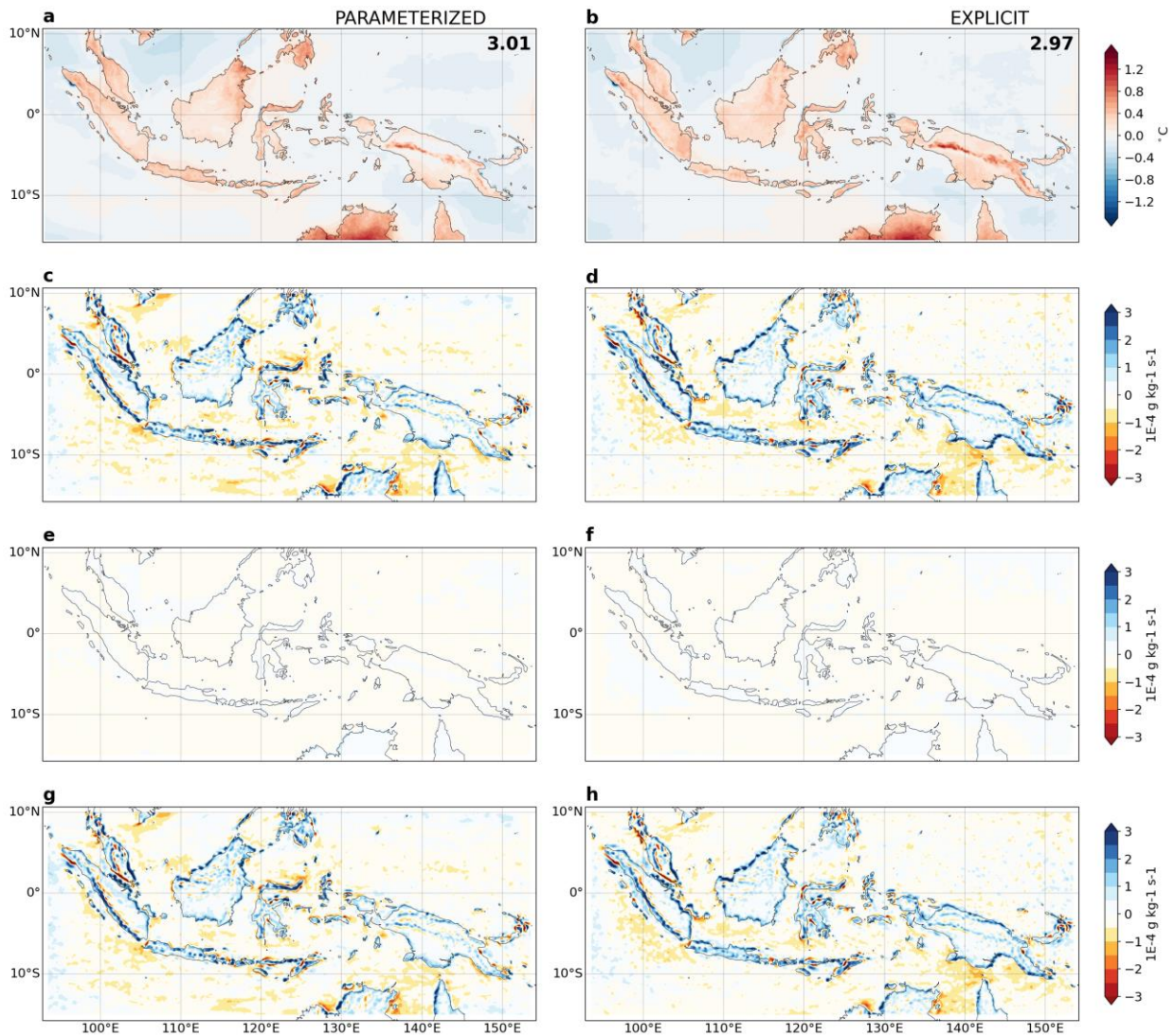
Figure 5: Near-surface temperature (2 m) changes with respect to the domain average warming (top-left numbers in panels a and b) over the entire period (NDJF 2013-2016) for parameterized (a) and fully explicit (b) convection runs. Changes in near-surface moisture flux convergence (spatially smoothed using a gaussian filter with standard deviation of 3 grid points) for parameterized (c) and fully explicit (d) experiments. Changes in MFC due to advection changes (e, f) and convergence changes (g, h) following decomposition in *Banacos and Schulzt* [2005].
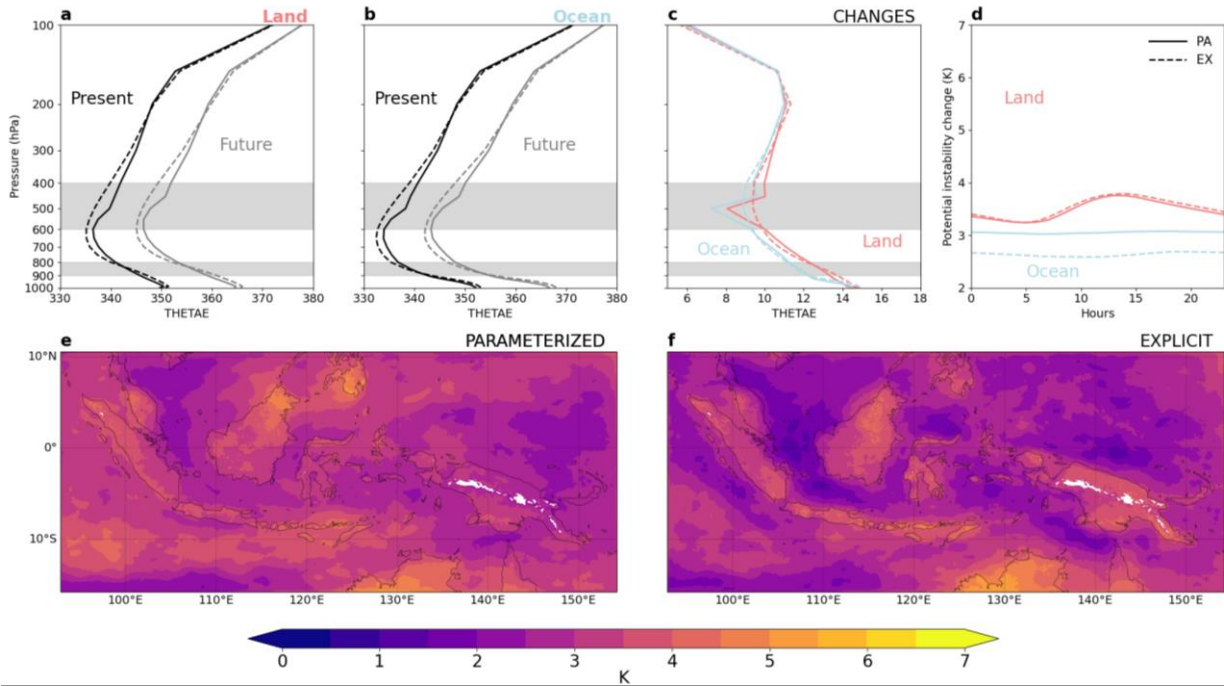
Figure 6: Atmospheric potential instability changes in parameterized and explicit convection runs. Time-averaged mean vertical profiles of θ_e over land grid points (a) and ocean grid points (b) and their changes (future minus present) (c). Black is for present climate and gray for future climate. Blue lines are changes over water only and red lines are changes over land only. Solid lines show parameterized convection experiments and dashed lines are for explicit convection runs. Diurnal cycle (d) of potential instability changes ($\theta_e^{850hPa} - \theta_e^{500hPa}$) for ocean (blue) and land (red) grid-points, and parameterized (solid) and explicit (dashed) convection experiments. Spatial distribution of potential instability changes for the parameterized (e) and explicit (f) convection simulations. Changes were statistically significant at the 99% confidence level in all grid points according to a two-sided Mann-Whitney U test.
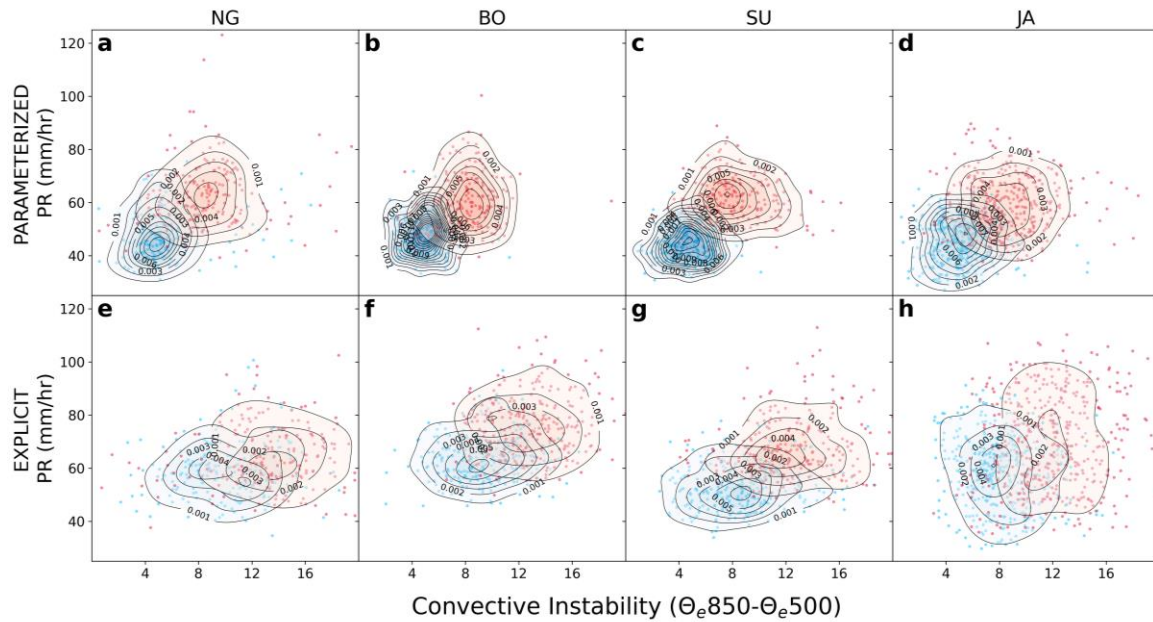
Figure 7: Extreme precipitation events (>99.9th percentile) versus convective instability in different locations for present (blue) and future (red) experiments using convective parameterization (PA, top row) and explicit convection (EX, bottom row). Convective instability is measured as the difference in equivalent potential temperature between the 900-800 hPa and 600-400 hPa layers and averaged over the 12 hours preceding the intense rainfall event. Each dot represents an event in the areas delimited by squares in Fig. 1 and the contours represents the probability estimated using a gaussian Kernel Density Estimator. All present and future point clouds are statistically different from each other using a Fasano-Franceschini test at the 0.01 significance level.
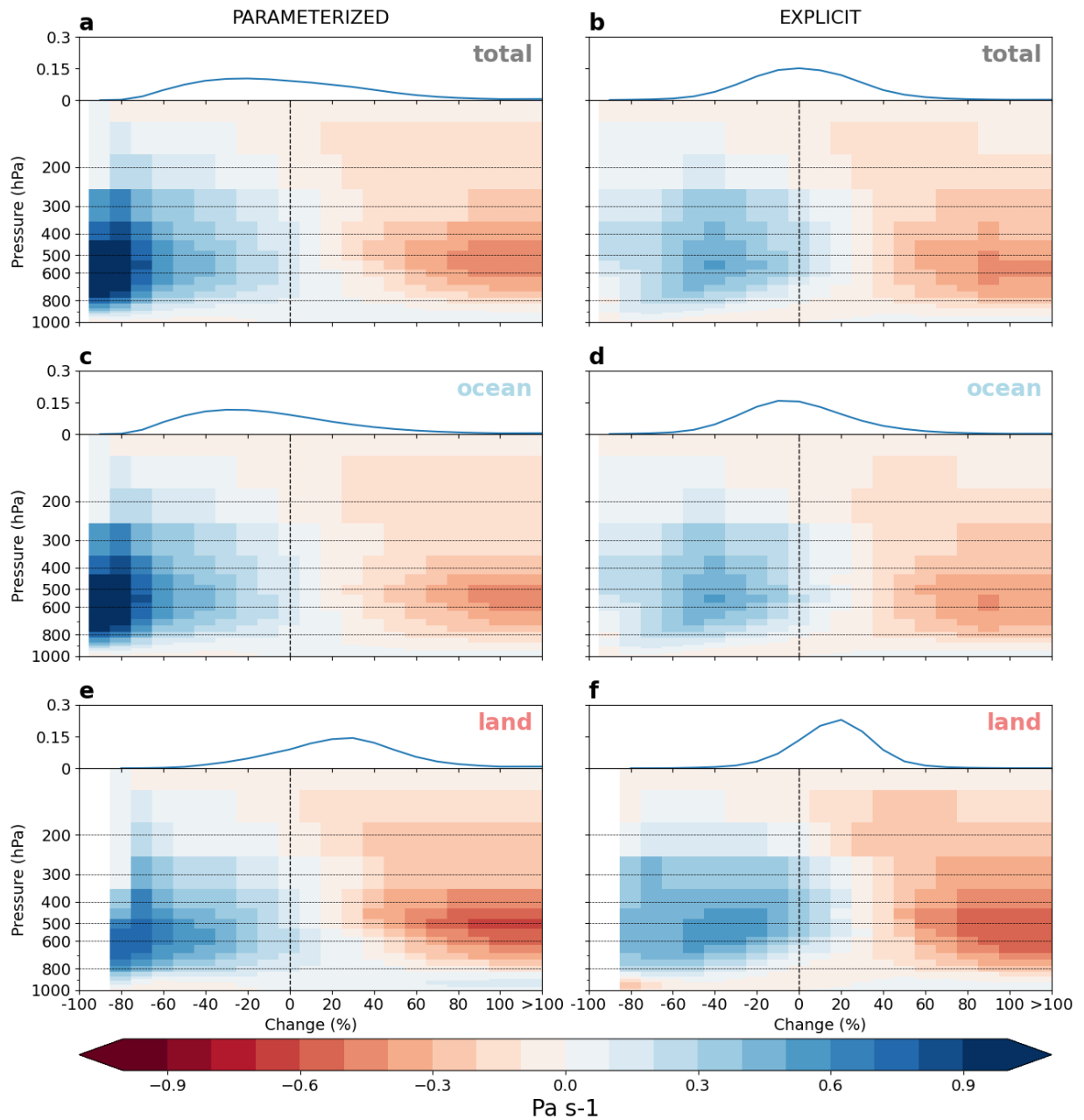
Figure 8: Changes in vertical pressure velocity (ω_e) versus changes in mean precipitation rates of events above the 99th percentile of hourly rainfall averaged over all (a, b), ocean-only (c, d) and land-only (e, f) grid points for the parameterized (left column) and the explicit (right column) convection experiments. Each panel includes a probability distribution of extreme precipitation changes at the top to indicate the most frequent values of changes in the domain.
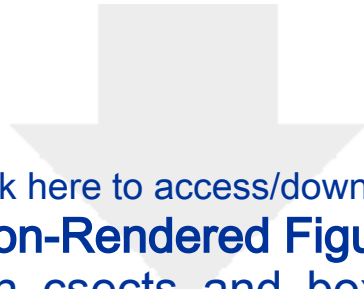
53

Click here to access/download
Supplemental Material
Supplementary_Argueso2021JCLIM.docx
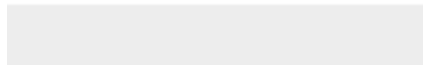
Figure 1

Figure 2

Click here to access/download
Non-Rendered Figure
Fig2_map_boxplot_meanR_CC_significance_v2.0_MWU
_masked_all.png

Figure 3

Click here to access/download
Non-Rendered Figure
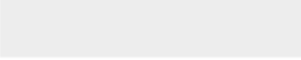Fig3_map_masked.png
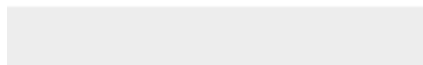
Figure 4
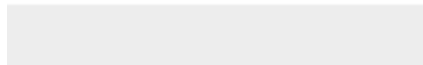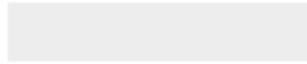
Figure 5

Figure 6

Click here to access/download
Non-Rendered Figure
Fig6_vprof_LANDOCEAN_statstabmap_THETAE_CC_pl
evs.png

Figure 7

Click here to access/download
Non-Rendered Figure
Fig7_ScatterPlot_PR99.9th_vs_THETAE_0.5_12hours.png

Figure 8